Chapter 4: Methods and Other Results

The following sections describe methodology and some methods and results not described in the previous chapters. It covers the experimental setup in the field, details of processing and receiver function deconvolution methods (both frequency domain and time domain deconvolution), phases used for receiver functions (P, PP, PKP, and S/SKS), the stacking method to obtain interface depths and the Vp/Vs ratio from receiver functions, the use of transverse receiver functions to look at anisotropy and dipping structures, imaging methods, finite difference modeling, and analysis of local events.

4.1: Field Work in Peru

Field work and installation of broadband seismic stations was performed which allowed for the collection of the data used for this study. Preparation for the installation of the first seismic array began in early 2008. The first array (Line 1) began collecting data at the end of June 2008. Line 1 was installed in collaboration with CENS at UCLA (Center for Embedded Networked Systems). Some of the collaborators in the field work were Richard Guy, Igor Stubailo, Emily Foote, and Allan Husker from UCLA/CENS, Jennifer Sery from Strassbourg France, Victor Aguilar from IGP, and Steve Skinner from Caltech. The first array was connected by a wireless system of YAGI and parabolic antennas so that seismic data could be automatically sent to central collection points and uploaded to a server in California via internet. The advantage of

this was that the data is immediately available which allows for quick detection and correction of problematic stations.

4.1.1 Installation Procedure

The seismic equipment was to be installed on the property of local residents for security purposes to reduce the likelihood of equipment being stolen. The first array, called Line 1 was planned to include a total of 50 stations over a distance of 300 km from Mollendo on the coast to Juliaca near Lake Titicaca allowing for a station spacing of 6 km. One of the installation challenges was that sites needed to be able to "see" each other in order to relay signals via YAGI or parabolic antennas. This required very careful site selection and sometimes antennas needed to be placed at greater heights or have their signal amplified in order to reach other stations.

After site permissions and selection, sites were prepared by digging holes for the sensor and metal box which contains the battery, digitizers (Quanterra Q330 and Reftek 130), and datalogger or CDCC (CENS Data Communication Controller) (Husker et al, 2008). Sites were connected to electricity either through solar panels or electrical connections to the local resident's power connection. For later arrays solar panels were used almost exclusively because of issues with power going out, particularly at places such as schools which close on holidays. Masts were also installed on the ground or roof to hold YAGI antennas and solar panels. Broadband Guralp 3T sensors were installed in a circular tube or trash can on top of a cement platform. The trashcan would be filled with an insulator. Examples of sites can be seen in figure 4.1. The arrays for Line 1 typically had an equipment box which was buried in the ground while for the other

arrays the box was attached to the solar panel mast either at the ground or partway up the mast.

 Figure 4.1: Photos from the installation of the seismic arrays. The sensor is places in the round holes where a blue trashcan is visible. It is seated in a cement base and insulated. Power in these cases is supplied by solar panel, and the box containing equipment is either attached to the base of the mast (left), attached halfway up the mast (center), or buried in the ground (right).

4.1.2 Second and Third Arrays

The second and third arrays began collecting data at the end of 2009 and 2010 respectively. Line 2 was installed between Cusco and Juliaca with about 50 stations imported from the Mexican MASE project (Middle America Subduction Experiment). The array distance and station spacing was comparable to Line 1. A significant difference between these arrays and the first array is that there was no need to connect the sites wirelessly which streamlined station installation. All seismic data is stored on memory cards and collected each month.

The stations for the third array were populated in a two stage process. First half of the stations from Line 1 were removed in mid-2010 and placed along Line 3. In mid-2011 half of the stations from Line 2 were removed to form the rest of Line 3. Thus when

Line 3 was fully operational in 2011 there were still stations collecting data on Lines 1 and 2. Line 3 is parallel to Line 1 and runs over a distance of 400 km. A few stations from the PULSE experiment which expand the line towards Brazil were later added which bring the total length covered up to 500 km.

4.2: Processing Methods and Receiver Function Methods

Events to analyze were selected according to distance and magnitude criteria. In total, about 232 events were used for receiver function analysis of Line 1 (80 using the P phase, 152 PP, and 52 PKP), 219 events for Line 2 (65 P, 154 PP, and 62 PKP), 178 events for Line 3 (57 P, 121 PP, and 27 PKP). For the stations on the coast between Mollendo and Nazca 61 events were used (19 P, 42 PP, and 13 PKP). For the CAUGHT/PULSE stations 46 events were used (19 P, 27 PP and 11 PKP).
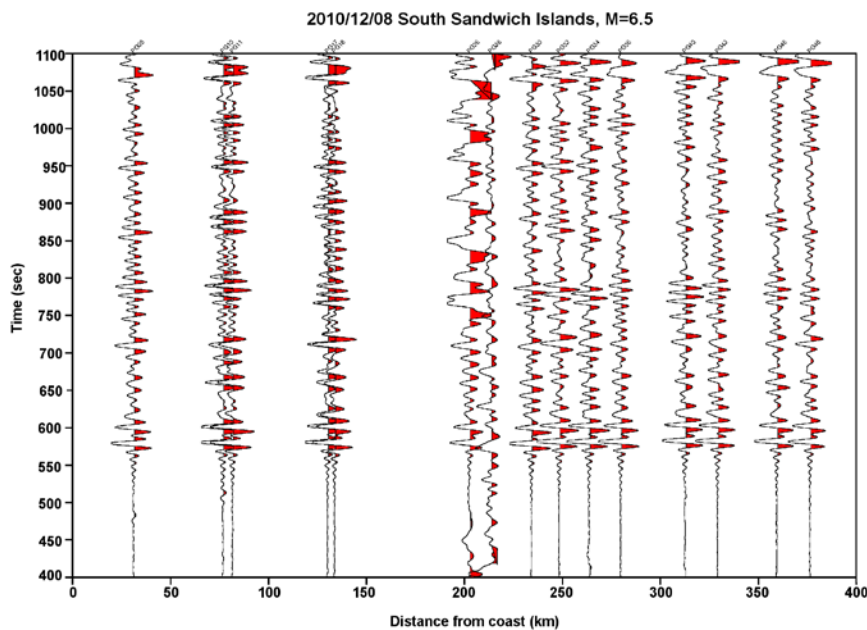

Figure 4.2: Data from the vertical component of seismograms recorded by Line 3 for a Mw 6.5 in Sandwich Islands on 12/08/2010.

Events were first bandpass filtered between 0.01 and 1 Hz or between 0.01 and 0.5 Hz depending on data quality. A significant portion of the data in Peru has a high amount of noise due to the large number of microseisms and seismic activity in Peru. Consequently for many events the signal from the earthquake is not even visible until after the data has been filtered. An example of a less noisy event can be seen in figure 4.2 which shows vertical seismograms recorded by Line 3 for a magnitude 6.5 event on 2010/12/08 in the S. Sandwich Islands region to the south of Peru. Figure 4.3A shows a comparison between an unfiltered trace (black), a trace filtered from 1 to 100 sec (red), and a trace filtered from 2 to 100 sec (green). Figure 4.3B shows the data prior to filtering (which has very low noise) and figure 4.3C shows the same traces after filtering (2 to 100 seconds). In both cases the P wave arrival can be clearly seen. There is bad data for one of the stations. Stations which consistently provide problematic data for a one-month period (the time between data collection trips) are reported and manually checked for issues in Peru at the next collection time. Often the vertical component will look normal, but one or more of the horizontal components of the seismogram will be problematic. This can be an issue for making receiver functions which require using both the radial and vertical components for deconvolution since sometimes at least a third or more of the stations will have one or more components that are bad. Such problems can usually be resolved by fixing any GPS errors and recentering the sensor mass when one or more channels is observed to be at an extreme value.
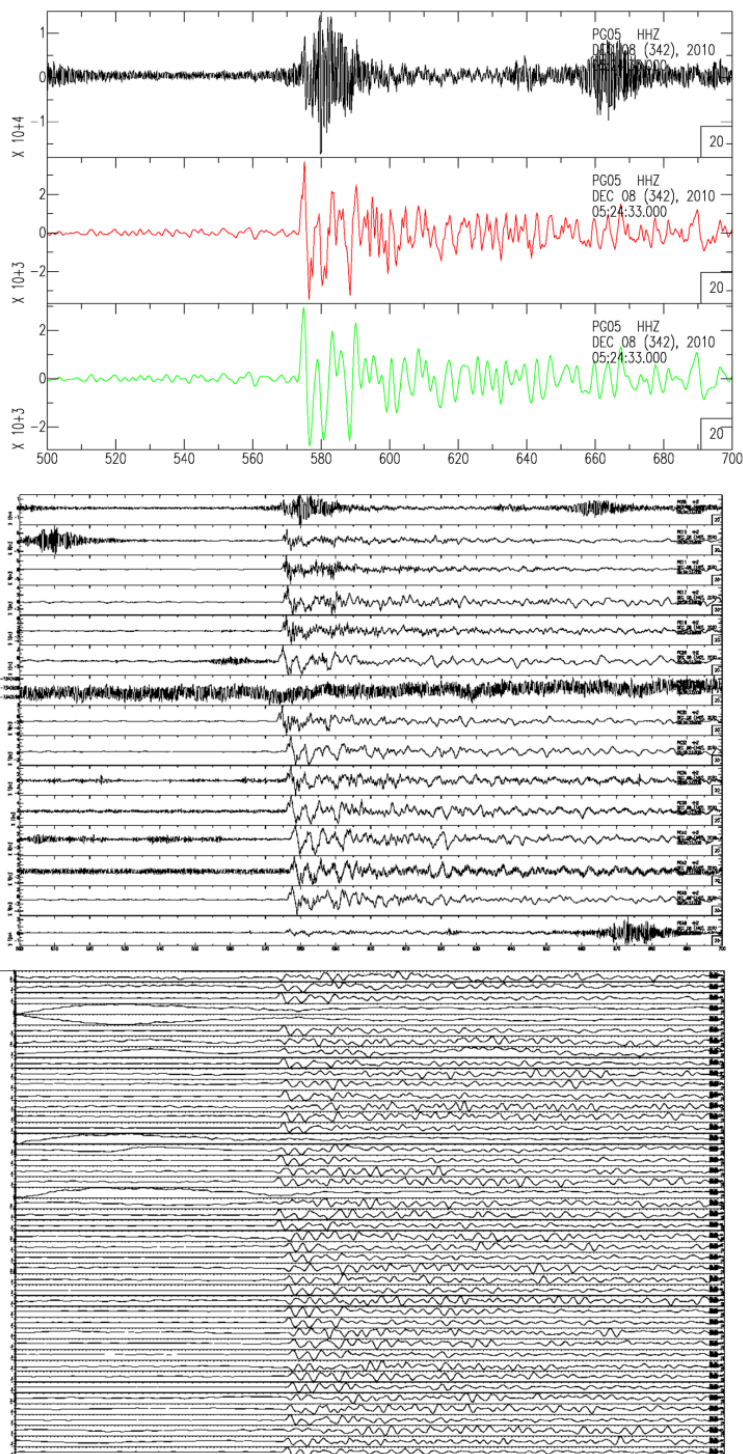
Figure 4.3: Comparison of unbandpassed data from 12/08/2010 recorded by Line 3 with data bandpassed to 1 second or 2 seconds. Top: Comparison of the vertical seismic component for PG05 unfiltered, bandpassed to 1 second, and bandpassed to 2 seconds.

Middle: All stations for 12/08/2010 unfiltered. Bottom: All Line 3 stations filtered to 2 second for 12/08/2010.

A comparison of receiver functions using 1 sec filtered data versus 2 sec filtered data is seen in figure 4.4. The major arrivals are the same in both cases although the 1 sec receiver function results can appear slightly higher in frequency. Any minor differences for individual stations result from choice of water level which is normally constrained by noise level. During the deconvolution part of receiver function analysis, values for water level parameter and gauss parameter are chosen based on quality, noise, and frequency content of receiver function results to obtain the highest quality receiver functions possible. The choice of gauss parameter (by default either 5 or 2.5) generally has little to no effect on results but can reduce the amount of artificial high frequency content if present. The choice of water level is by default 0.01 unless the receiver function results are noisier in which case 0.1 would be selected. For particularly good results 0.001 is used.
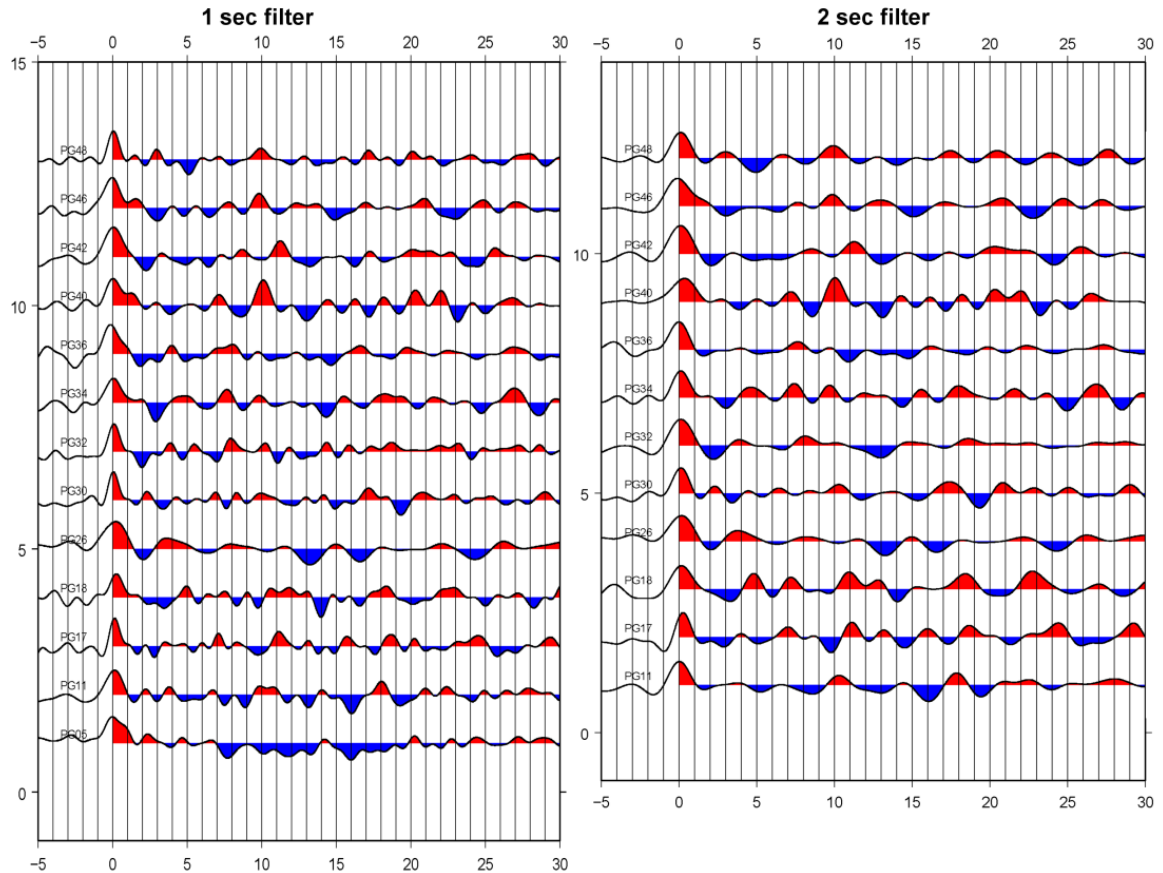
Figure 4.4: Comparison of receiver functions for 12/08/2010 Sandwich Islands bandpassed to 1 second (left) and 2 seconds (right). Individual stations have very similar receiver functions and consistent main arrivals regardless of the filtering. Receiver functions bandpassed to the higher frequencies tend to be slightly noisier.

4.2.1: Processing Procedure

Event information added to SAC headers if each data file comes from the Southern

California Earthquake Data Center using STP (Seismic Transfer Program). After the

origin time has been set, the P wave arrival time is estimated using an automatic picker

which uses the event distance and depth and a standard velocity model (IASP91). The

data is cut to 100 sec before the P wave arrival and 300 sec after the P arrival and then

the set of three components for each station is individually checked for quality and

accuracy of the automatic arrival pick. If the picks are observed to be inaccurate they can be picked manually but small adjustments to the P arrival time were not found to have a significant impact on the receiver functions. The data that passes the quality control test is rotated into vertical, radial, and tangential directions.

4.2.2 Deconvolution methods

4.2.2.1 Frequency Domain Deconvolution

Most receiver functions shown here are done using frequency domain deconvolution although time domain deconvolution was also done. The basic procedure can be found in Langston, 1979. In the time domain the theoretical displacement response can be written as:

$$DV(t) = I(t) * S(t) * E_V(t), \qquad (4.1)$$

$$DR(t) = I(t) * S(t) * E_R(t), \qquad (4.2)$$

$$DT(t) = I(t) * S(t) * E_T(t), \qquad (4.3)$$

where I(t) is the instrument impulse response, S(t) is a complicated source time function, and $E_V(t)$, $E_R(t)$, $E_T(t)$ are the structure impulse response in the vertical, radial, and tangential directions. Langston, (1979) citing Burdick and Helmberger, (1974) noted an observation from teleseismic data "that the vertical component of ground motion behaves as a pulselike time function convolved with the instrument response with only minor later arrivals." This resulted in the approximation I(t)*S(t) ~ D_V(t) which assumes that D_V(t) behaves as a dirac delta function. Thus in the frequency domain:

$$ER(\omega) = \frac{D_R(\omega)}{I(\omega)S(\omega)} \sim \frac{D_R(\omega)}{D_V(\omega)}, \qquad (4.4)$$

$$ER(\omega) = \frac{D_R(\omega)}{I(\omega)S(\omega)} \sim \frac{D_R(\omega)}{D_V(\omega)}. \qquad (4.5)$$

This receiver function deconvolution process removes source effects and mantle

propagation effects to give only information about structure directly beneath the station.

Due to numerical instability in the above equations, the following form is used:

$$ER(\omega) = \frac{D_R(\omega)D_V^T}{\max\{D_V(\omega)D_V^T, \; c \; \cdot \max[D_V(\omega)D_V^T]\}} \; G(\omega), \qquad (4.6)$$

where in the previous equation the superscript T represents taking the transpose, c is the

water level parameter, and G is the Gaussian function of the form $G(\omega) = e^{-\omega^2/4\alpha^2}$

where α is the Gauss parameter.

The resultant receiver function has a large arrival from the direct P wave at t = 0

followed by an arrival from the converted phase, usually a P to S conversion at the

Moho, followed later by multiple arrivals.

4.2.2.2. Time Domain Deconvolution

Deconvolution in the time domain is an iterative approach which was described in

Ligorria and Ammon (1999) as a "least-squares minimization of the difference between

the observed horizontal seismogram and a predicted difference between the observed

horizontal seismogram and a predicted signal generated by the convolution of an

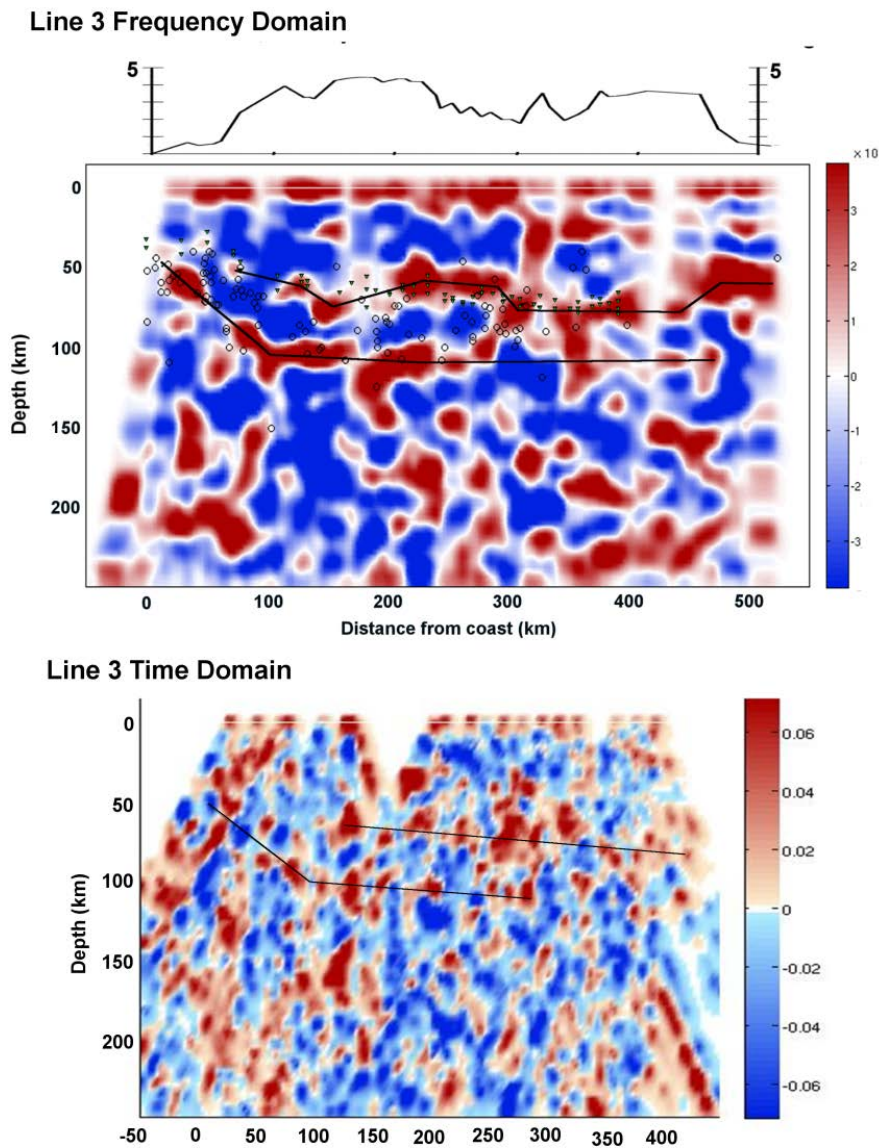iteratively updated spike train with the vertical-component seismogram."

Figure 4.5: Receiver function images for Line 3 from backprojection of receiver functions using events from a NW backazimuth. The top image contains receiver functions made with frequency domain deconvolution while the bottom image has receiver functions made with iterative time domain deconvolution. Black lines show the approximate locations of the slab and Moho from the images. Note that the top image has a longer distance scale due to the addition of stations from the PULSE experiment which were analyzed with frequency domain deconvolution. Station elevation is shown at the top of the figure.

CCP stacks, Frequency domain deconvolution
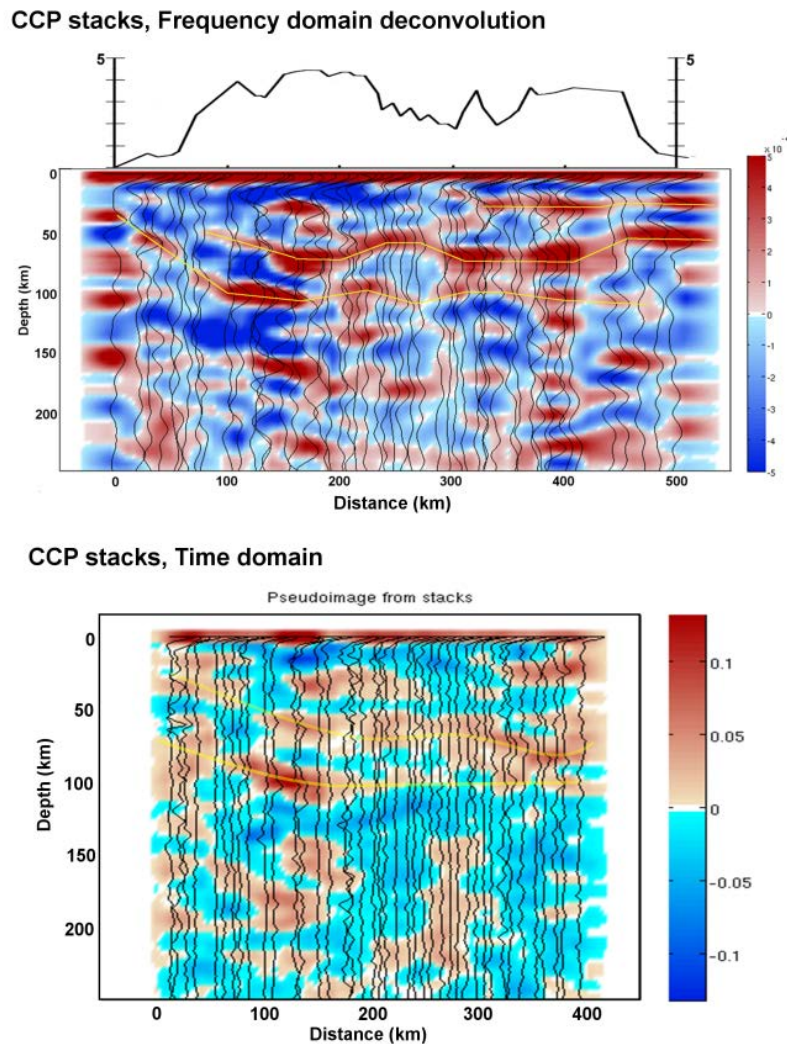

CCP stacks, Time domain

Figure 4.6: A comparison of receiver function images in the frequency domain and time domain using CCP (common conversion point) stacking for events from a NW backazimuth. The Moho and slab shape are more defined for the time domain RFs when stacks are plotted rather than the unstacked data (as in figure 4.5).

Receiver functions using time domain deconvolution produce results consistent with those in the frequency domain but receiver function results shown in this chapter are based on frequency domain deconvolution due to a higher amount of noise in the time domain results (see figure 4.5 and figure 4.6 which show receiver function images

using both methods for Lines 1 and 3). A comparison of the receiver functions using time and frequency domain deconvolution methods can be seen in figure 4.7 which shows receiver functions from the event on 2012/12/08 earthquake in Sandwich Islands. A comparison of receiver functions from the same stations shows that in most cases, the positive and negative pulses match up well. The main difference is that the time domain receiver functions appear as sharp pulses while the frequency domain receiver functions are longer period.
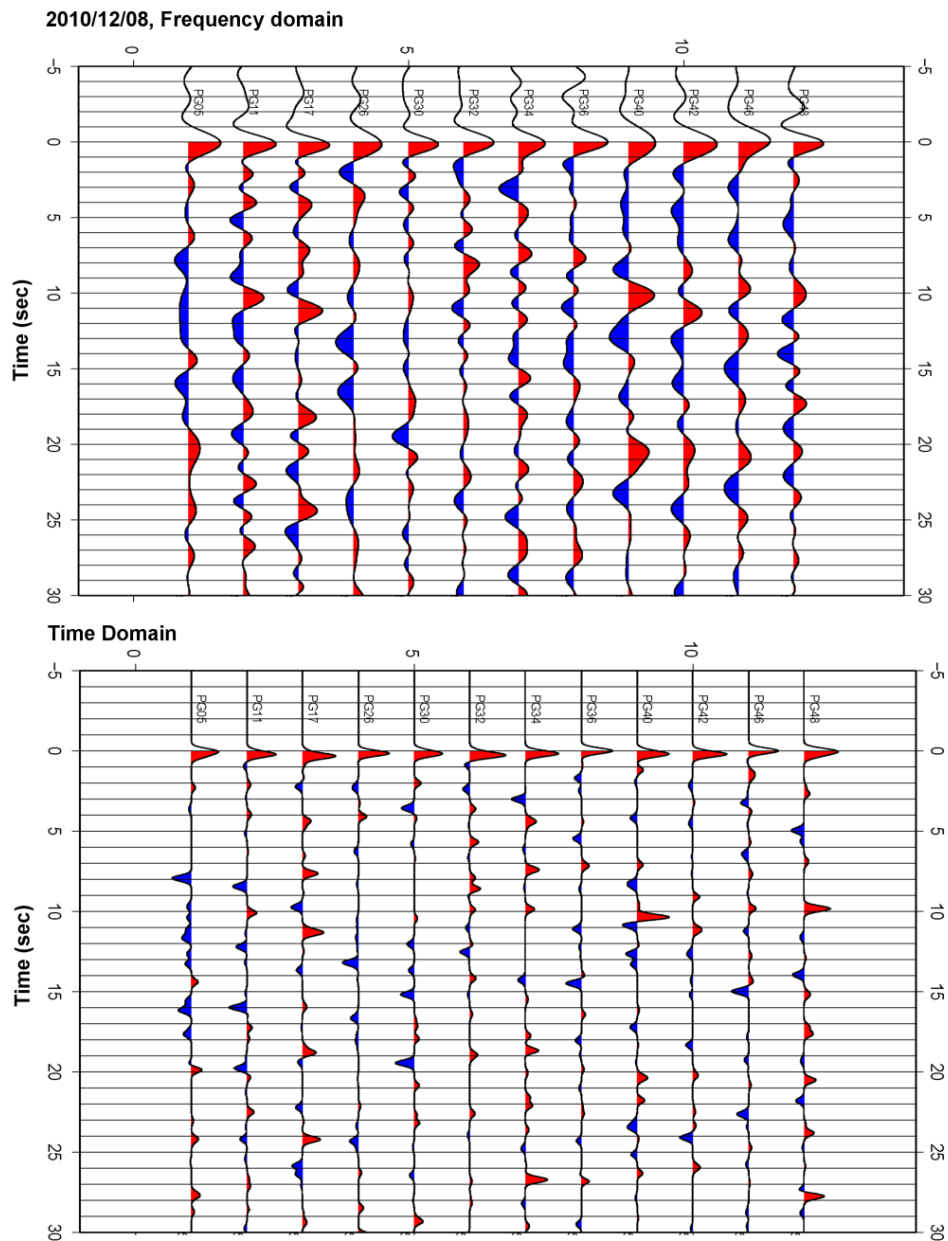
Figure 4.7: Receiver functions for 12/08/2010 Sandwich Islands event (data shown in figure 4.2) using frequency domain deconvolution (top) and time domain deconvolution (bottom). The main arrivals are seen to be consistent for both methods.

A comparison of the two methods for individual stations can be seen in figure 4.8 and

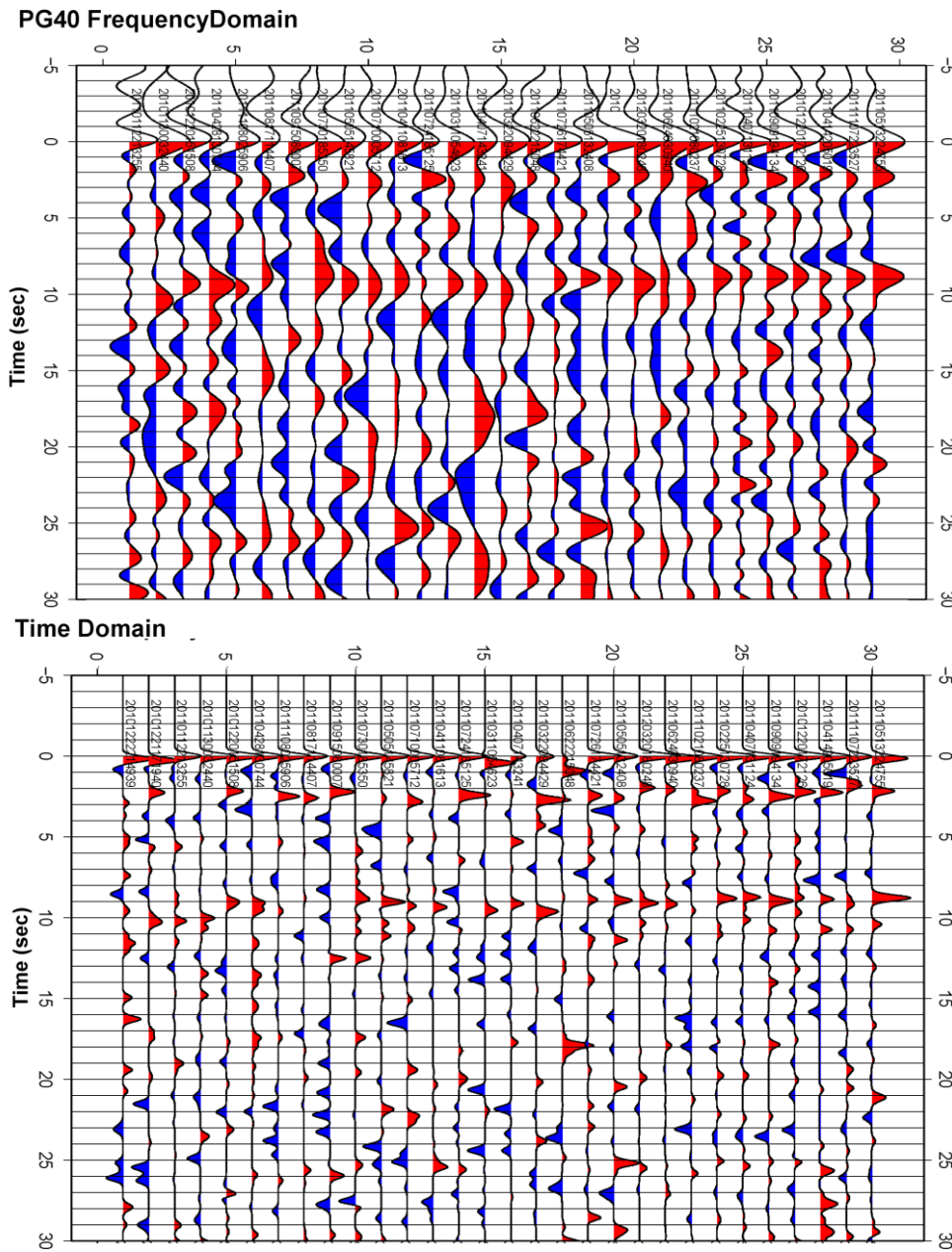figure 4.9 which show sample receiver functions for stations PG40 and PG50.

Figure 4.8: Comparison of time domain deconvolution (top) and frequency domain deconvolution (bottom) for station PG40 for earthquakes from a northwest backazimuth.
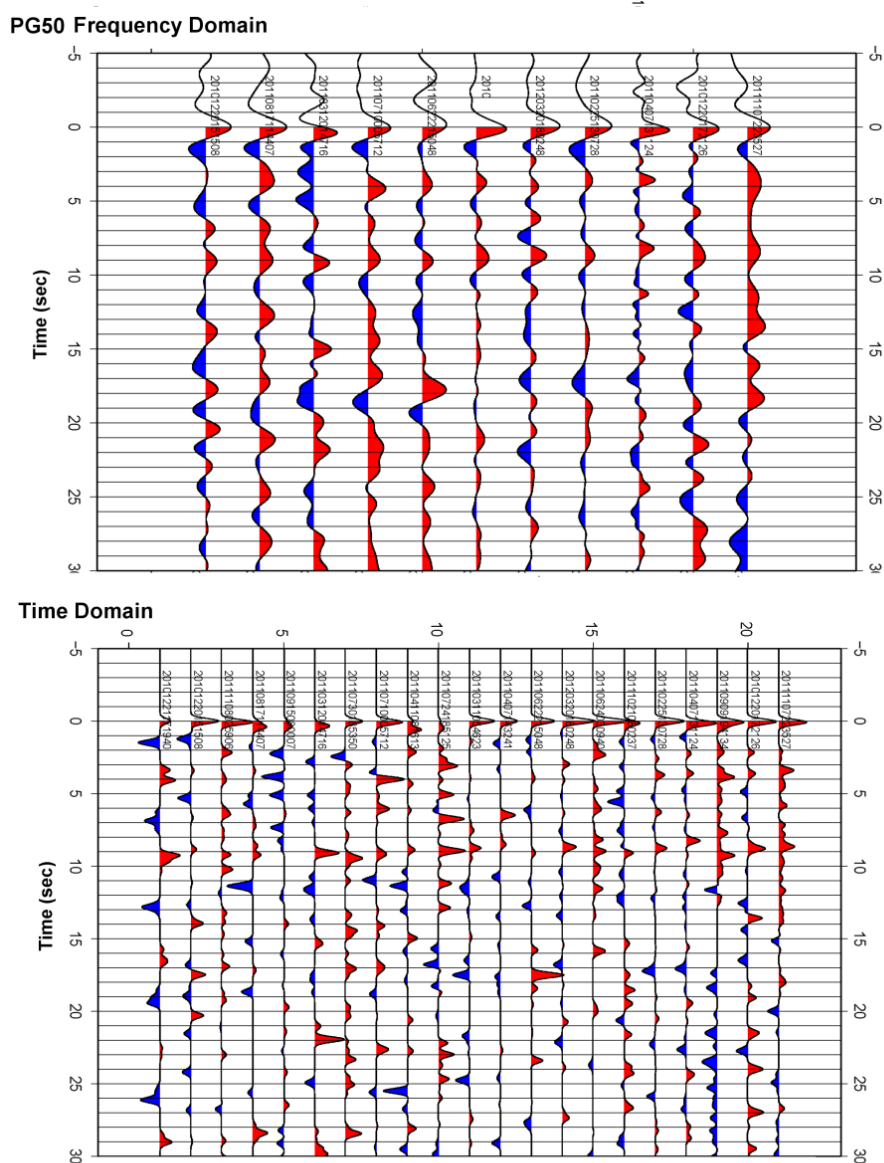
Figure 4.9 Comparison of time domain (top) and frequency domain (bottom) deconvolution for station PG50 using earthquakes from a northwest backazimuth.

4.3 Phases Used for RFs

4.3.1. P, PP, and PKP

Standard receiver functions are done using the P wave phase with distances between 30

and 90 degrees to avoid interference with crustal and core phases. However from the

location of Peru, many large events occur at greater distances from Peru which makes it useful to use phases such as PP or PKP. The PP phase is used for phases between 90 and 180 degrees while the use of PKP phases is limited to very distant events between 142 and 180 degrees. The magnitude ranges are greater than 5.8 for P wave phases, greater than 6.0 for events between 90 and 142 degrees, and greater than 6.3 for events more distant than 142 degrees. The use of the PP phase is not uncommon in receiver function studies (Julià et al, 2008; Frassetto et al, 2010). The PKP phase has also been used for detection of dipping interfaces (Endrun et al, 2004; Lucente et al, 2005) but is less standard than PP and P phases. Due to the almost vertical arrival angle of PKP core phases, we do not expect to see a strong conversion at flat interfaces however PKP phases are good for recognizing dipping interfaces such as the slab dipping at 30 degrees in the normal subduction region. Receiver functions using the P phase on the other hand are better if the flat layer approximation is met. However the receiver function method can be adapted to account for dipping interfaces (Zhang & Langston, 1995). Thus using all possible phases results in better event and azimuthal coverage and can account well for both dipping and flat interfaces. The receiver function deconvolution procedure used for PP and PKP is the same as in the case of the P phase except for using the time difference between the PP/PKP phase and the P to S converted phase at an interface for that same arrival. For most of the events the P and PKPdf phase are easily recognizable, but there is often more noise around the PP and PKPab phases so careful event and receiver function selection is needed to ensure high quality results. Figure 4.10 shows all available events from station PE46 on Line 1

from a NW azimuthal direction to Peru. The figure shows overall consistency in timing
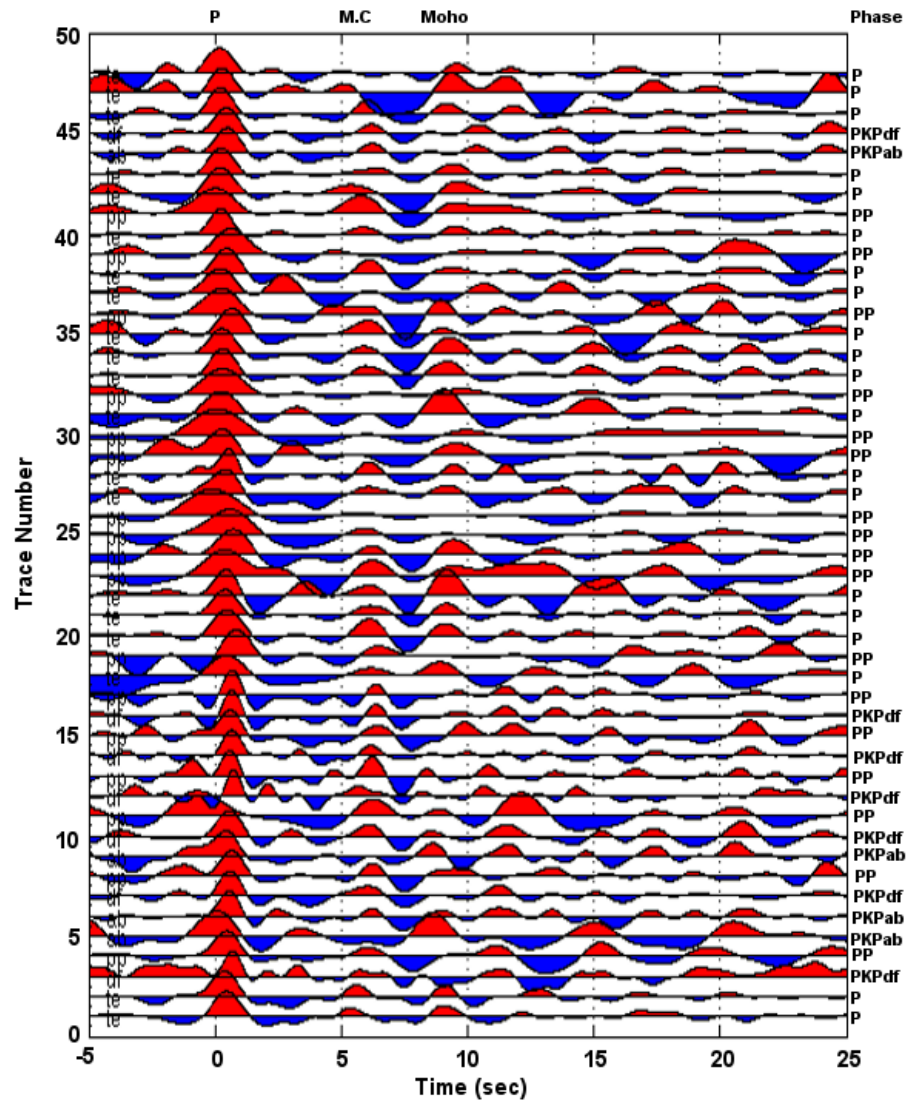
for major arrivals.

Figure 4.10: Receiver functions for station PE46 from a northwest backazimuth. Receiver functions based on the P phase (for distances 30-90 degrees), PP phase (events greater than 90 degrees), and PKPab or PKPdf phase (events greater than 142 degrees) are included. The midcrustal structure and Moho can be seen clearly. All phases appear consistent for the crustal arrivals.

Stacking receiver functions for each station from a similar backazimuth can reduce noise and help bring out the strongest and most consistent arrivals. Similar stacking approaches such as CCP or common conversion point stacking result in similar quality improvements. Despite the similarity between the results using different phases, for analysis purposes receiver functions based on the P or PP phase are separated from the PKP phase, and some difference can be seen particularly in the conversion at the top of the slab as seen in figure 4.11. The figure shows an image from Line 1 (using CCP stacking of P/PP receiver functions from the NW backazimuth) compared with an image using the PKP phases from the direction of Indonesia. The black line shows the expected slab location based on seismicity in the Wadati-Benioff zone. In the case of the P/PP phases, the top of the subducting slab is marked by a strong positive pulse which is expected at the base of the oceanic crust where there is a velocity increase from the subducting oceanic crust to the mantle. The velocity jump from the mantle wedge to the top of the oceanic crust is expected to produce a negative pulse in the receiver functions. The PKP images shows the expected slab location marked by a change from negative to positive impedance however the signal as an opposite polarity as the P/PP image. The images are seen to match up well in terms of the slab signal if the PKP image is inverted. The polarity difference between the P and PKP phases has also been noted in Lucente et al, (2005).
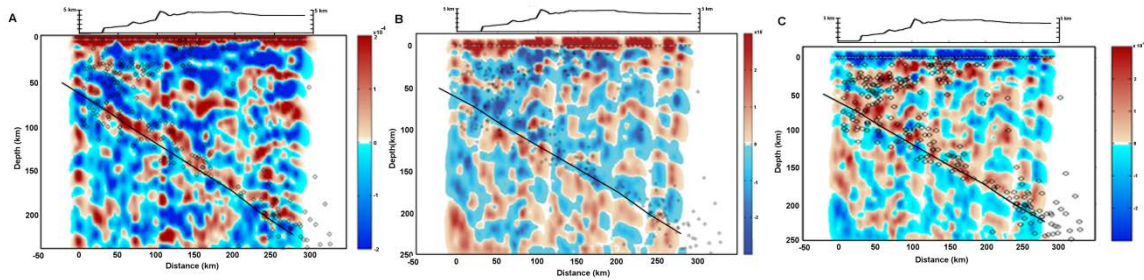
Figure 4.11: Left: Receiver function image for Line 1 using CCP stacking of P and PP receiver functions showing a clear positive impedance signal associated with the subducting slab and the Moho. Middle: PKP image with backprojected receiver functions from the direction of Indonesia. A signal from the slab appears as a change from negative to positive impedance. Arrivals are out of phase with the P/PP results (as mentioned in Lucente et al, 2005). Right: Inversion of the PKP image in the center. Here the positive arrival associated with the slab matches up with the P/PP observations.

4.3.2.   S Wave RFs

Receiver functions were made based on the S and SKS waves although analysis is more complicated compared to P phases and results are longer period in general and thus do not provide high resolution. However several studies using S waves have been done (Geissler et al, 2010; Heit et al, 2007, Kumar et al, 2005) which suggest that S wave receiver functions can be useful for detecting the lithosphere-asthenosphere boundary which is generally not detectable by P receiver functions. While the calculation of P wave receiver functions involve rotating the horizontal components into the radial and tangential directions, S waves receiver functions are optimized by rotation into the P-SV-SH coordinate system.   Several different methods were tested for finding an optimum rotation angle starting from the radial and tangential directions. One method involved rotating by the angle of incidence for the S wave arrival using the ray parameter and average S wave velocity in the crust. A comparable result should be

obtainable by finding an angle that minimizes the energy at the time of the S wave on

the P component. The third method used equation (21) from Kennett, (1991) which

provides an approximation for the rotation for slowness bands appropriate for S-wave

phases involving use of the Hilbert transform of the vertical component to estimate the

P-wave contribution. The general form for the rotation is the free surface transfer

matrix from Kennett (1991):

$$
\begin{bmatrix} P \\ SV \\ SH \end{bmatrix} = \begin{vmatrix} \dfrac{(\beta^2 p^2 - \frac{1}{2})}{\alpha q_\alpha} & \dfrac{p\beta^2}{\alpha} & 0 \\ p\beta & \dfrac{(\frac{1}{2}-\beta^2 p^2)}{\beta q_\beta} & 0 \\ 0 & 0 & \dfrac{1}{2} \end{vmatrix} \begin{bmatrix} Z \\ R \\ T \end{bmatrix} \tag{4.7}
$$

where $q_\alpha=(\alpha^{-2}-p^2)^{0.5}$, $q_\beta=(\beta^{-2}-p^2)^{0.5}$.

The method which was empirically found to produce the best S-wave receiver functions

was the method using the angle of incidence to perform the rotation.   After performing

the rotation, the deconvolution method is similar to the P wave deconvolution in the

frequency domain except that since we are looking for a S wave converting to a P

wave, the vertical component (SV component) is divided by the horizontal component

(P component) rather than the other way around.   Sample results using the S wave

phase can be seen in figure 4.12. A wide region of negative impedance marks the

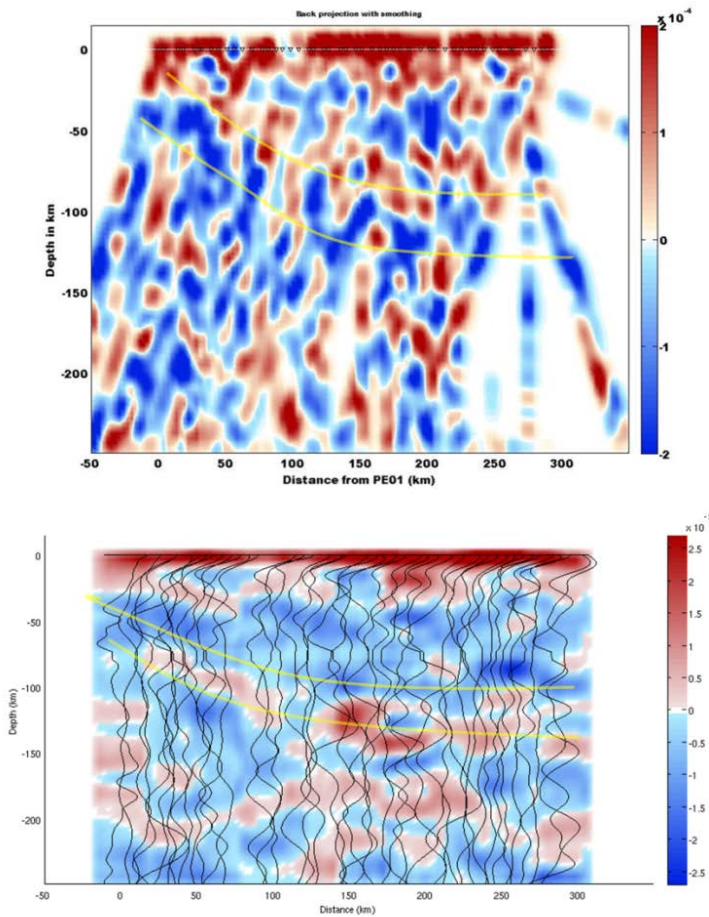general location of the lithosphere-asthenosphere boundary.

Figure 4.12: S wave receiver function images for Line 1. The location of the LAB is expected to appear as a negative signal. Results for the S wave are longer period than P wave results. The top image is based on backprojection while the bottom image plots stacks for each station.

4.4 Stacking for Moho Depth and Vp/Vs

When an adequate number of receiver functions have been obtained from a given

azimuthal direction, receiver functions can be stacked for each station using the method

of Zhu & Kanamori, (2000) to obtain an estimate for depth to an impedance contrast

and average Vp/Vs for that region. Depth and Vp/Vs can be estimated through the

following equations which contain p (the ray parameter) and t_{Ps}, t_{PpPs}, $t_{PpSs+PsPs}$ which
are the times for the converted phase and multiple arrivals relative to the direct P arrival
(at time = 0).

$$H = \frac{t_{Ps}}{(\sqrt{\frac{1}{V_s^2} - p^2} - \sqrt{\frac{1}{V_p^2} - p^2})} \tag{4.8}$$

$$H = \frac{t_{PpPs}}{(\sqrt{\frac{1}{V_s^2} - p^2} + \sqrt{\frac{1}{V_p^2} - p^2})} \tag{4.9}$$

$$H = \frac{t_{PpSs+PsPs}}{2\sqrt{\frac{1}{V_s^2} - p^2}} \tag{4.10}$$

The estimations are done through a grid search algorithm over a range of possible
depths and Vp/Vs ratios, and the optimum parameters are those that maximize the
summation of receiver function amplitudes at the time of the converted arrival (Moho
signal) and weighted summations of amplitudes for the calculated multiples. Due to the
large variation in Moho depth over the arrays from around 30 to 75 km depth beneath
the Altiplano, the average crustal Vp is expected to vary slightly. Velocities are
estimated from spacial averages of the 3D model by Cunningham & Roecker (1986)
(see figure A2 in appendix A). An example of this can be seen in figure 4.13 (and also
figure 2.6). Results from this stacking for Moho and Vp/Vs can be seen in figure 2.8
and figure 3.9.

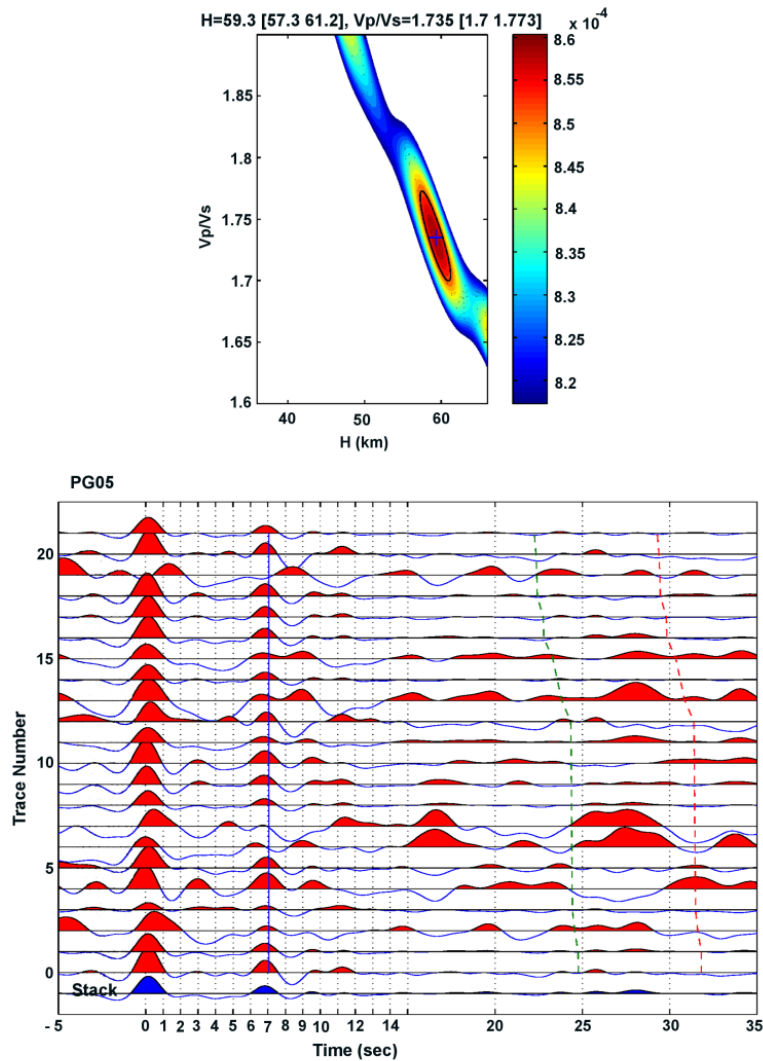Figure 4.13. An example of the grid search (top) and stacking (bottom) to find Moho depth and Vp/Vs for station PG05. In the top portion, H is the depth to the impedance contrast. In the bottom portion, the blue line represents the time at which the maximum summation is obtained for the Ps converted phase and multiple arrivals (denoted as dashed lines). In this case the signal from the Moho is very clear, but the multiples are not readily apparent.

4.5 Transverse Receiver Function Components

The receiver function method produces both radial and transverse components.

Although all of the receiver function images shown in previous chapters only use the

radial component, energy on the transverse receiver function component can be indicative of either dipping structures or anisotropy. In a flat, homogeneous setting, the amplitude of arrivals on the transverse component should be very small relative to the radial receiver functions. Several studies have used transverse receiver function components to examine dipping structures or anisotropy (Zhang & Langston, 1995; Savage, 1998). According to Savage, (1998), "transversely anisotropic systems with horizontal symmetry axes have waveforms with 180˚ periodicity as a function of back azimuth, while dipping symmetry axes or dipping boundaries just have 360˚ periodicity." Thus if the anisotropic symmetry axes is roughly horizontal, stacking transverse receiver functions from 180˚ apart can provide an indication of whether there is dipping or anisotropic structure based on whether resulting amplitudes increase or decrease in the stack.

An analysis of transverse receiver functions shows more energy on the transverse components for Line 2 (parallel to the trench) compared to other stations. In many cases the signal amplitude is comparable to the amplitude of the radial receiver functions. Two examples of transverse and radial receiver functions for stations PF25 and PF37 can be seen in figure 4.14 and figure 4.15.
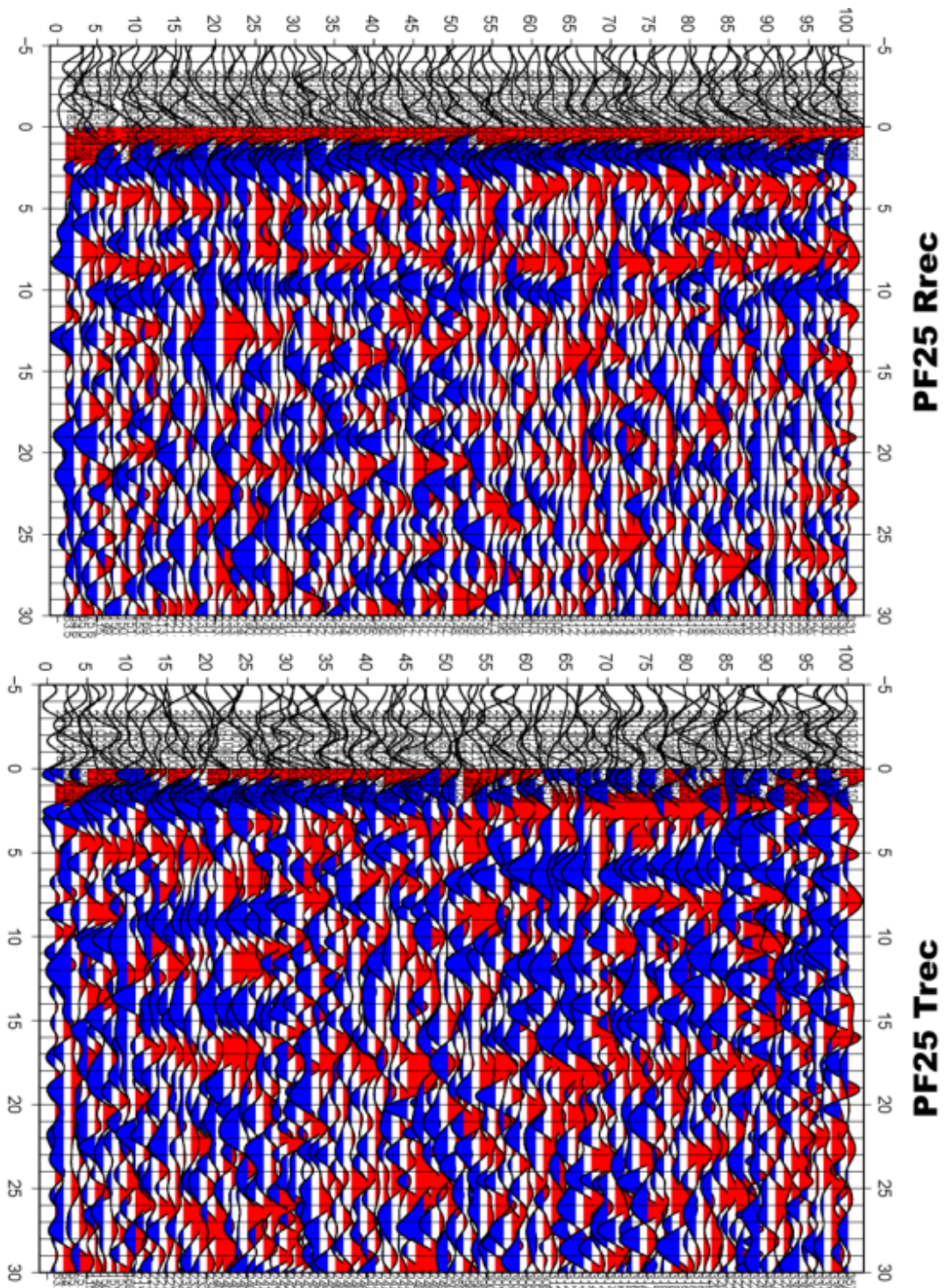
Figure 4.14. Comparison of the radial and transverse receiver function components for station PF25. The most coherent energy on the transverse receiver functions generally occurs before 10 seconds which is where the crustal signals are observed on the radial component. On the radial receiver functions, positive signals at 4-5 seconds and at about 8 seconds correspond to the midcrustal structure and Moho signal respectively.
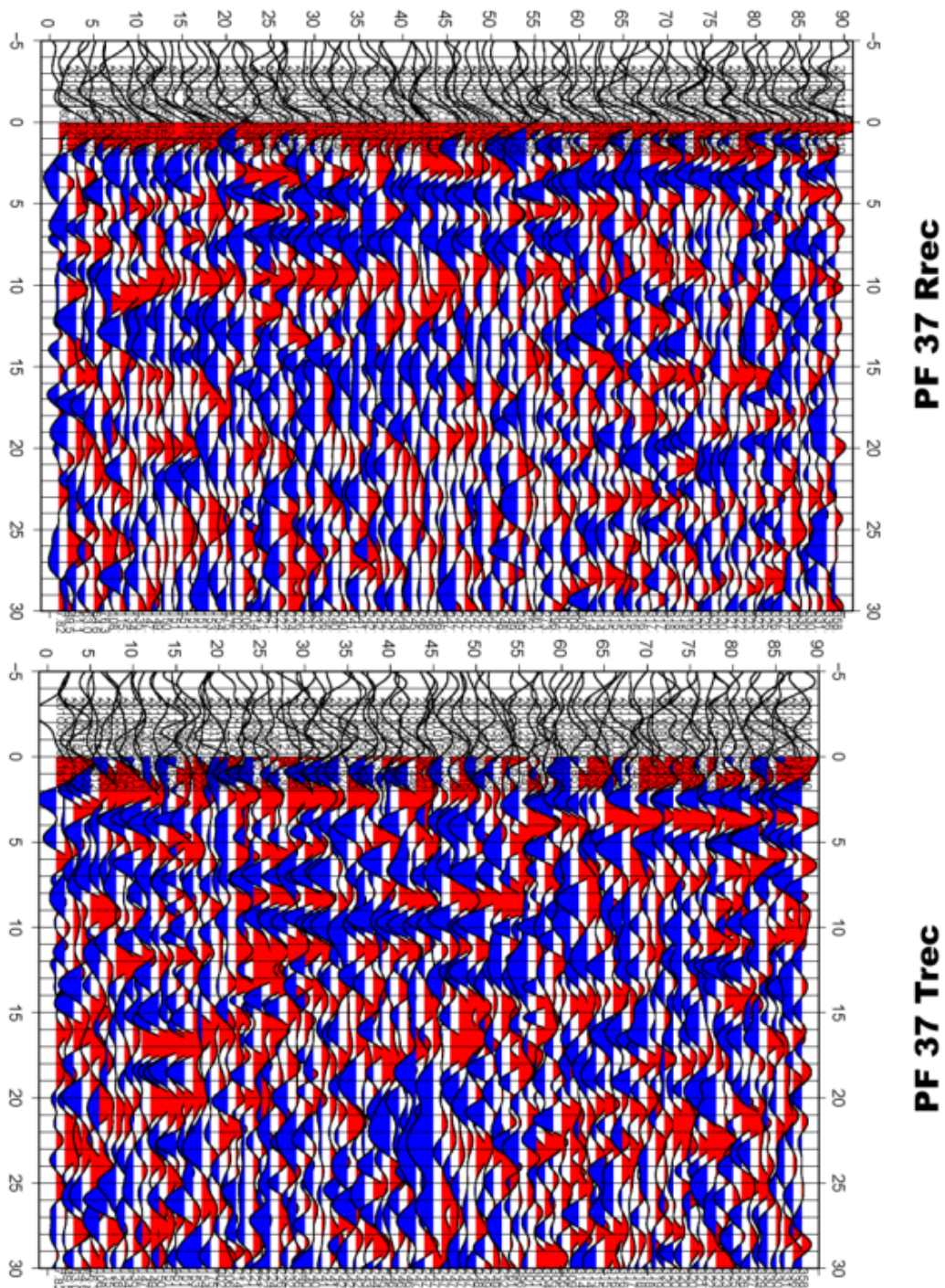
Figure 4.15. Comparison of the radial and transverse receiver functions for station PF37. Energy on the transverse component has an amplitude comparable to the main arrivals on the radial receiver function (besides the P arrival).

Transverse receiver functions from 30˚ azimuthal regions were stacked to check for 180˚ or 360˚ periodicity. Most of the teleseismic energy comes from the directions NW, NE, SW, and SE from Peru. Comparisons of transverse signals from the NW with energy from the SE and similarly from the NE with the SW shows that major arrivals have opposite polarity from directions 180˚ apart for all stations examined (figure 4.16, figure 4.17, and more examples in appendix C). This appears to indicate that there is possibly some anisotropy.
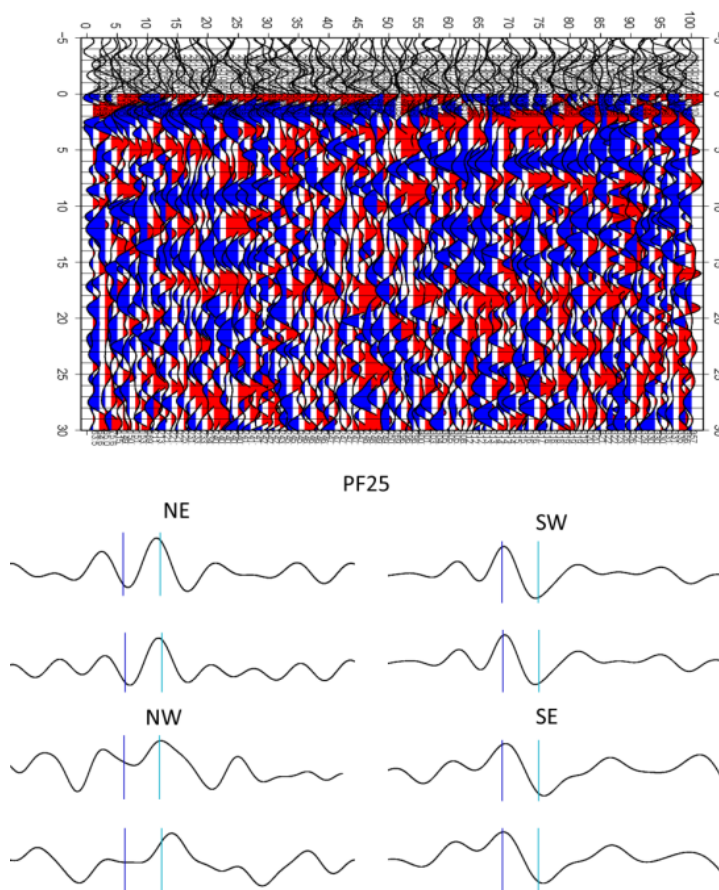

Figure 4.16: Top: Transverse RFs for station PF25. Bottom: Stacks of all transverse receiver functions from the directions NE, SW, NW, and SE. Each trace represents a stack over a region of 30 degrees which includes at least three transverse RFs.
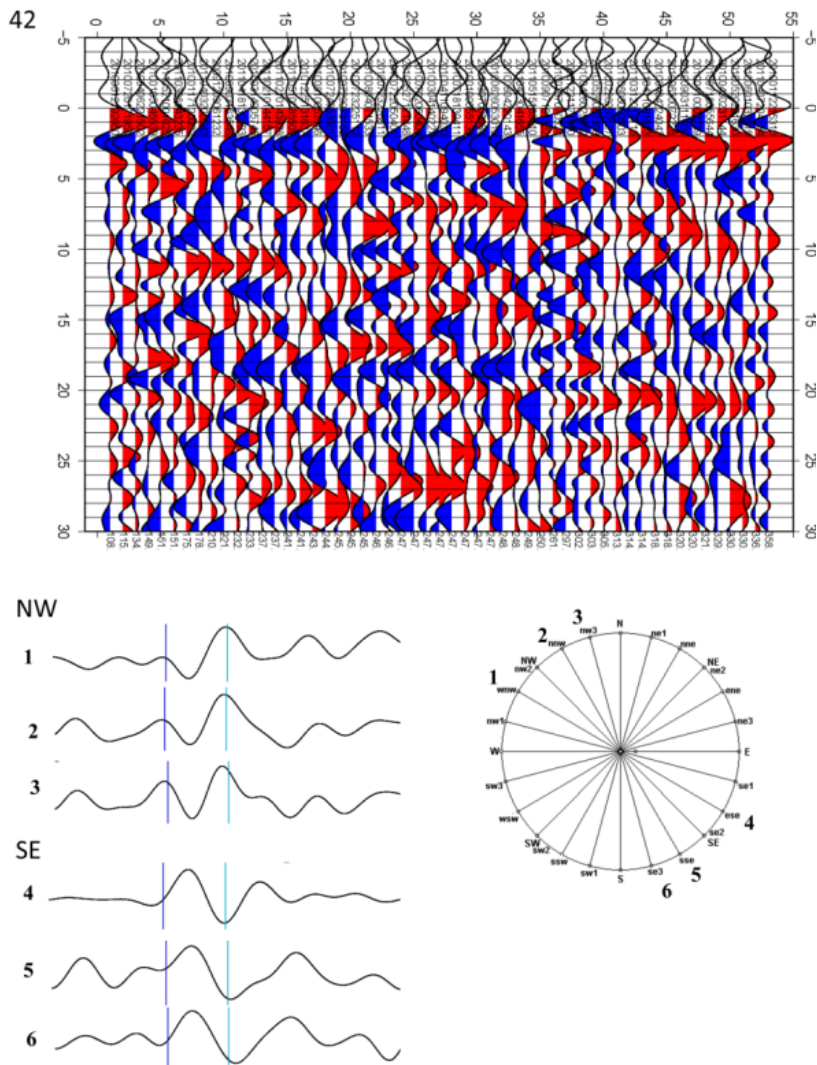
Figure 4.17: Transverse RFs for station PF42 and stacked traces from the directions noted on the unit circle to the NW and SE. The traces are marked at zero seconds (dark blue line) and the time of the first major arrival at about 2 seconds (light blue). Note the polarity difference between the NW and SE directions.

The direction of the symmetry axis appears to be between 260 and 296 degrees for the northwestern stations (closest to Cusco). The lack of energy from due west of Peru makes it difficult to further constrain the angle (a vast majority of earthquakes are from

either a NW or SW azimuth from Peru). See examples in figure 4.18 and figure 4.19

where the expected symmetry axis has been marked.   The symmetry angle appears

closer to 214˚ near the center of the lines (e.g., PF23 and PF24 in figure 4.20) and

perhaps closer to 150˚ for PF12 and PF13 closer to Juliaca (figure 4.21).
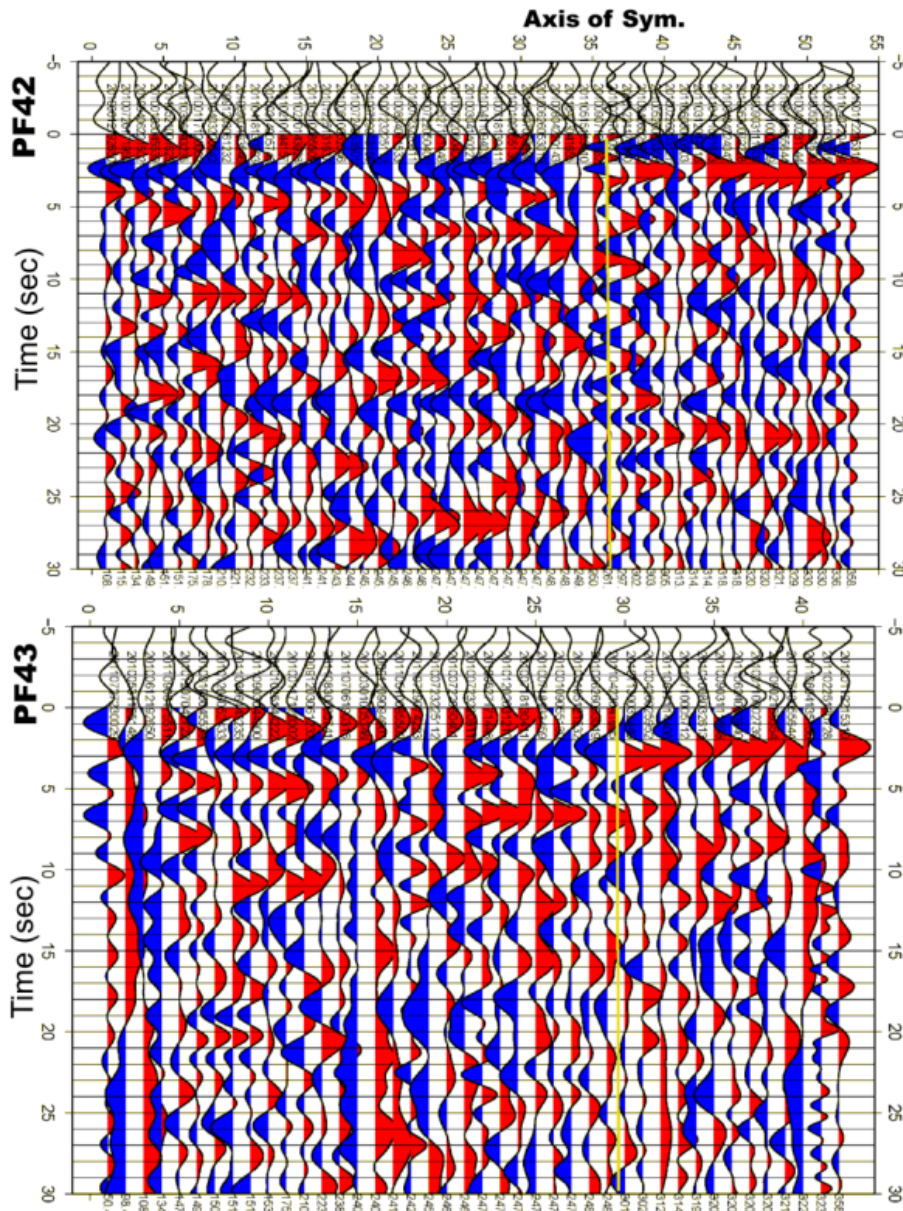
Figure 4.18: Transverse RFs for stations PF42 and PF43 with the
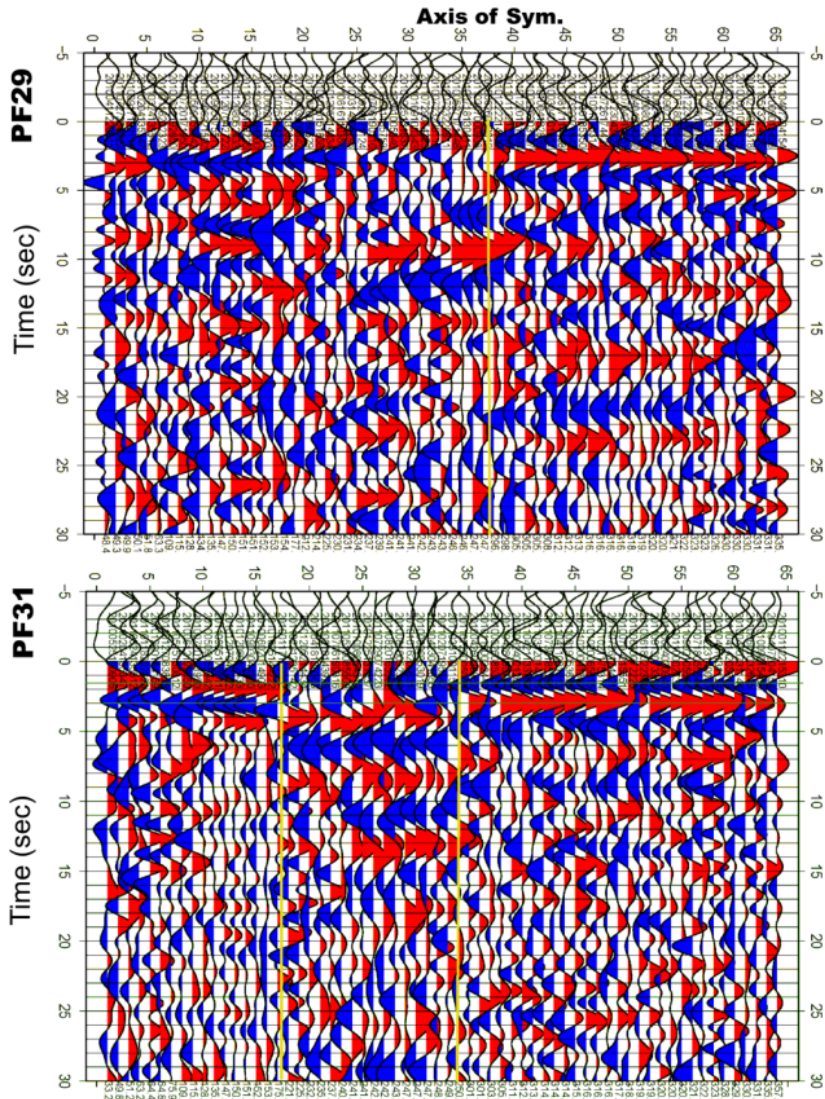Possible symmetry axis marked by the yellow line.

Figure 4.19 Transverse RFs for stations PF29 and PF31 with possible symmetry axis marked by the yellow line.
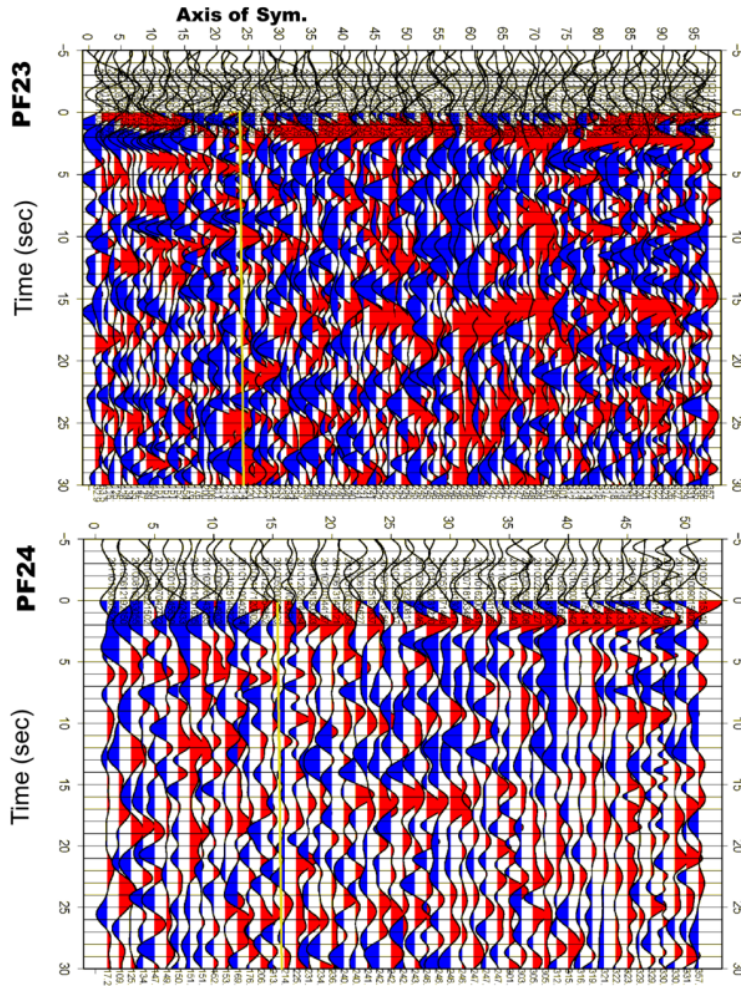
114

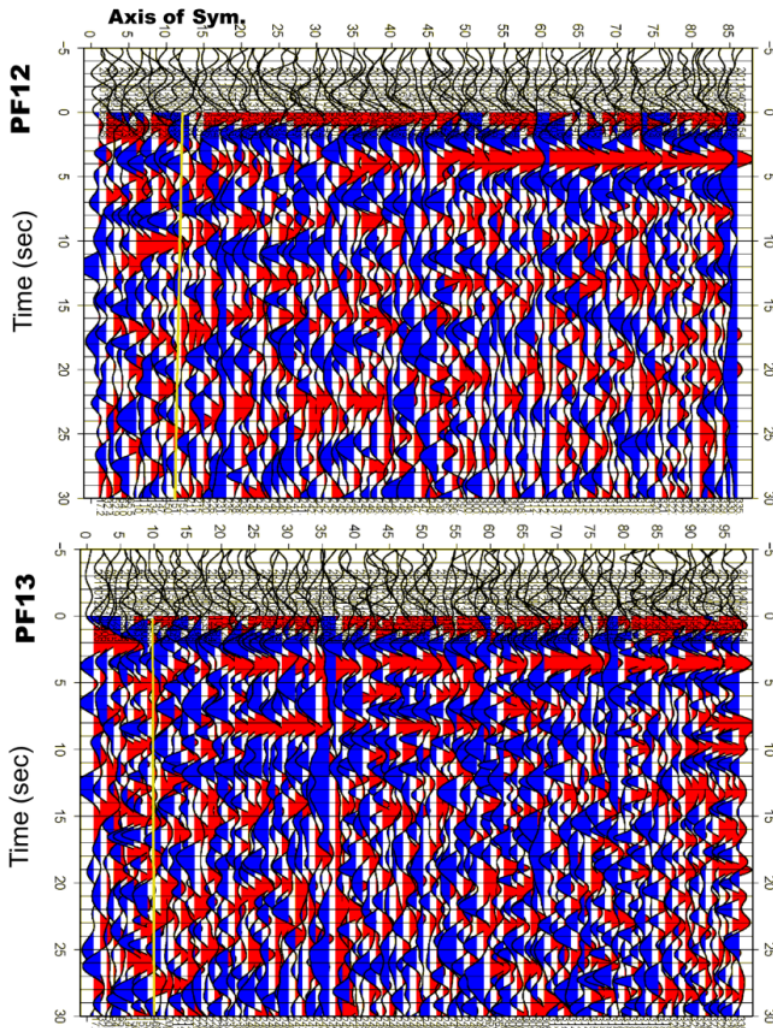Figure 4.20 Tranverse RFs for stations PF23 and PF24 (possible symmetry axis marked by yellow line).

Figure 4.21 Tranverse RFs for stations PF12 and PF13 (symmetry axis marked by yellow line).

Observations from radial receiver functions are that image quality can vary by azimuth but this is partly a function of fewer events from other directions besides NW and SW (such as W, E, S, N, NE, and SE). See an example of images from each major direction in figure 4.22 for Line 3. As seen from the images, the quality of images from the northern directions is generally better than using only events from southern directions.
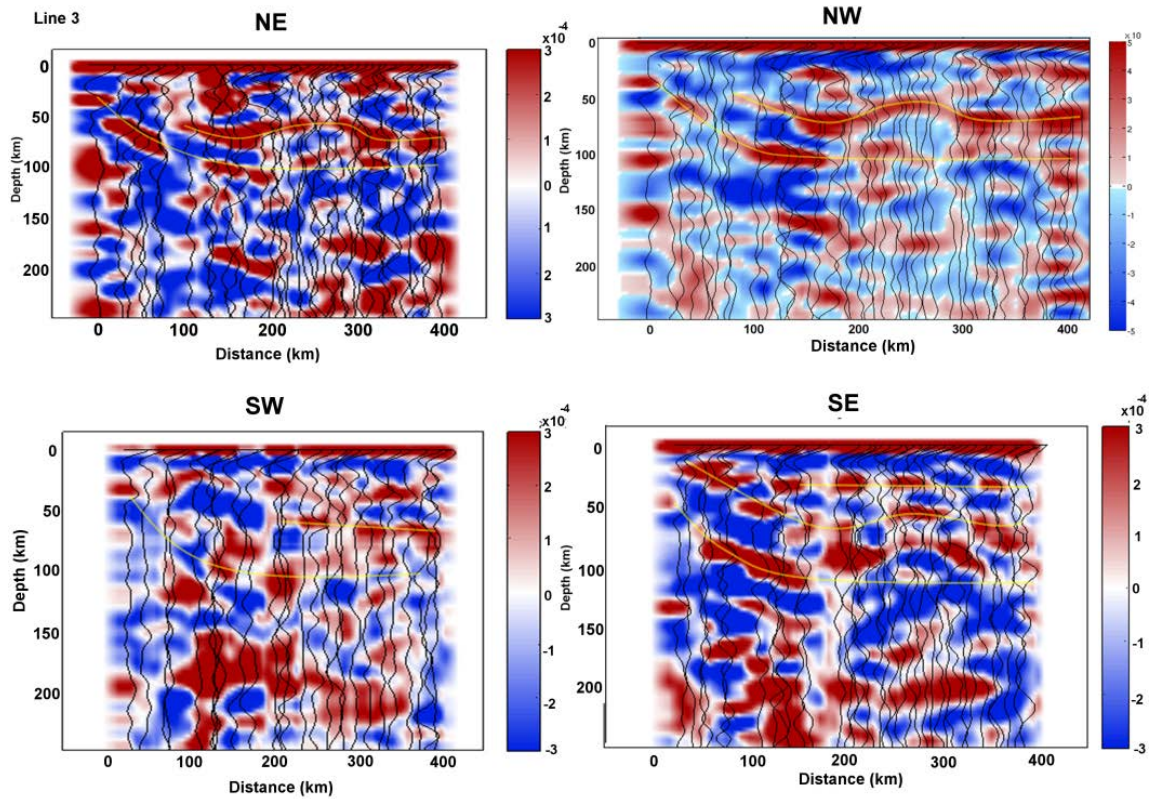
Figure 4.1 CCP stacks from each azimuthal direction for Line 3

4.6 Imaging Methods (Backprojection, CCP)

The backprojection method I developed uses a ray based approach to project receiver functions in the direction from which the energy originated. Distance is calculated from the first station in the array along the line between the first and last station in the array. A simple time to depth estimate is performed using the ray parameter, an average crustal velocity of 6.3 km/s, an average mantle velocity of 8.1, and average Moho depth of 40 km. The equation

$$depth = \frac{t_{(x)}}{(\sqrt{\frac{1}{V_{sc}^2} - p^2} - \sqrt{\frac{1}{V_{pc}^2} - p^2})} \quad (4.11)$$

is used for depths less than the Moho depth, and the equation

$$depth = \frac{t_{(x)} - H(\sqrt{\frac{1}{V_{sc}^2} - p^2} - \sqrt{\frac{1}{V_{sm}^2} - p^2} + \sqrt{\frac{1}{V_{pm}^2} - p^2} - \sqrt{\frac{1}{V_{pc}^2} - p^2})}{(\sqrt{\frac{1}{V_{sm}^2} - p^2} - \sqrt{\frac{1}{V_{pm}^2} - p^2})} \quad (4.12)$$

is used for depths greater than the Moho depth. The distance range depends on the

length of the array and the maximum depth is 250 km. The distance from the station is

calculated using a simple layered velocity model based on IASP91 where 0-10 km

depth has Vp=5.8km/s, 10-H depth has Vp=6.8 km/s, H-120km depth has Vp=8.045,

120-165 km depth has Vp=8.1 km/s, 165-210 km depth has Vp=8.25, and depths

greater than 210 km have Vp=8.45 where H is the Moho depth. The average Moho

depth is normally set to 40 km due to the amount of variation for Lines 1 and 3 from the

coast to the Altiplano but the model was varied using greater depths to test the

sensitivity of the images to the velocity model. The images and depths were found to

be consistent even when average Moho depth was changed to account for the greater

depths beneath the Altiplano. Using the simple layered velocity model, angles and

distances are calculated based on the depth in the model, ray parameter, geometry, and

Snell's law. The distance from the station is further corrected by taking into account

the backazimuthal direction of the event which affects the distance and direction that

rays are projected. The station elevation is also taken into account such that depth=0 is

sea level. Thus crustal thickness includes the Moho depth added to the station elevation

which for many places in the Altiplano can be up to 4 km. An example of applying

backprojection to a single station can be seen in figure 4.23 for PE46 on Line 1.

Comparison of the results to the CCP stacking image in figure 4.24 confirm that the

Moho and midcrustal structure and Moho depth are relatively flat in the region covered

by rays from station PE46. A moveout plot to the right of the backprojection image

shows receiver function coverage as a function of ray parameter. Signals from

interfaces such as the Moho are expected to be flat in such a plot while arrivals from

multiples can vary as a function of ray parameter. Further examples of figures using

backprojection can be seen in figures 2.7, 2.8, 2.9, and figures 3.6, 3.7B, and figure
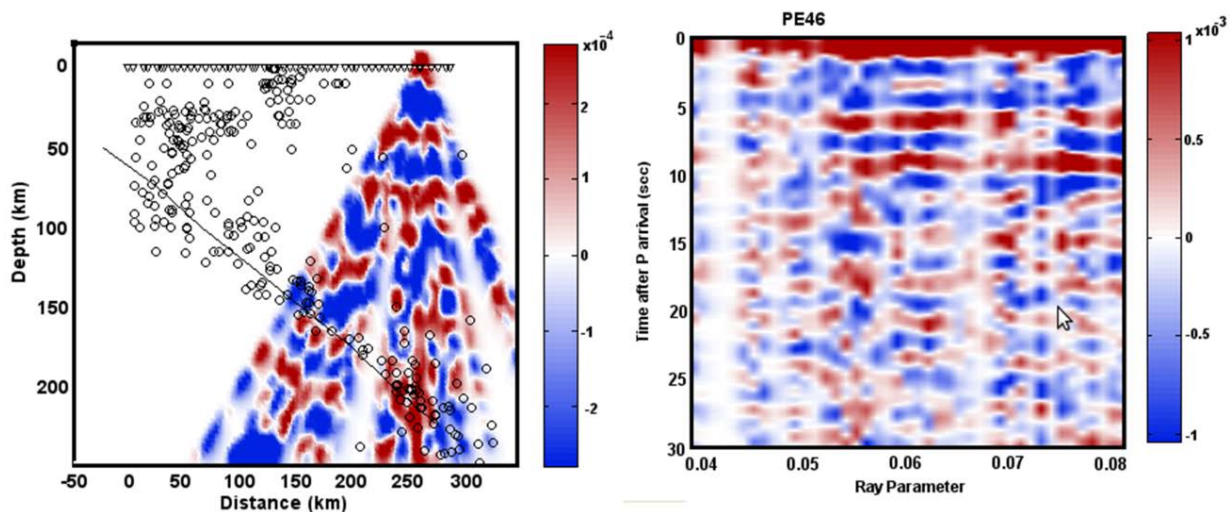
3.12.

Figure 4.23: Left: Results from backprojecting receiver functions for station PE46 near the end of Line 1 (closest to Juliaca) in the direction from which the energy originated. Right: Plot of time versus ray parameter where the color corresponds to the amplitude of the receiver functions at that ray parameter. Signals from the midcrustal structure (at ~5 seconds) and Moho (~9 seconds) are consistent across all azimuths.

The common conversion point method uses some of the techniques developed in the

backprojection approach but uses actual depths calculated for the Moho based on H-κ

stacking (Zhu and Kanamori, 2000) and finds the best-fitting polynomial function to create a smooth Moho function for any distance. It then calculates the distance and depth at which a backprojected ray intercepts the Moho depth. The distance along the array is broken into bins (which usually have a size equivalent to the station spacing) and the Moho intercept distance determines the bin number. All events which pass through the same bin are stacked and stacks are plotted as in figure 4.24 which shows CCP stacking results for Line 1. Further examples of figures using this method can be seen in figures 3.4 and 3.7.
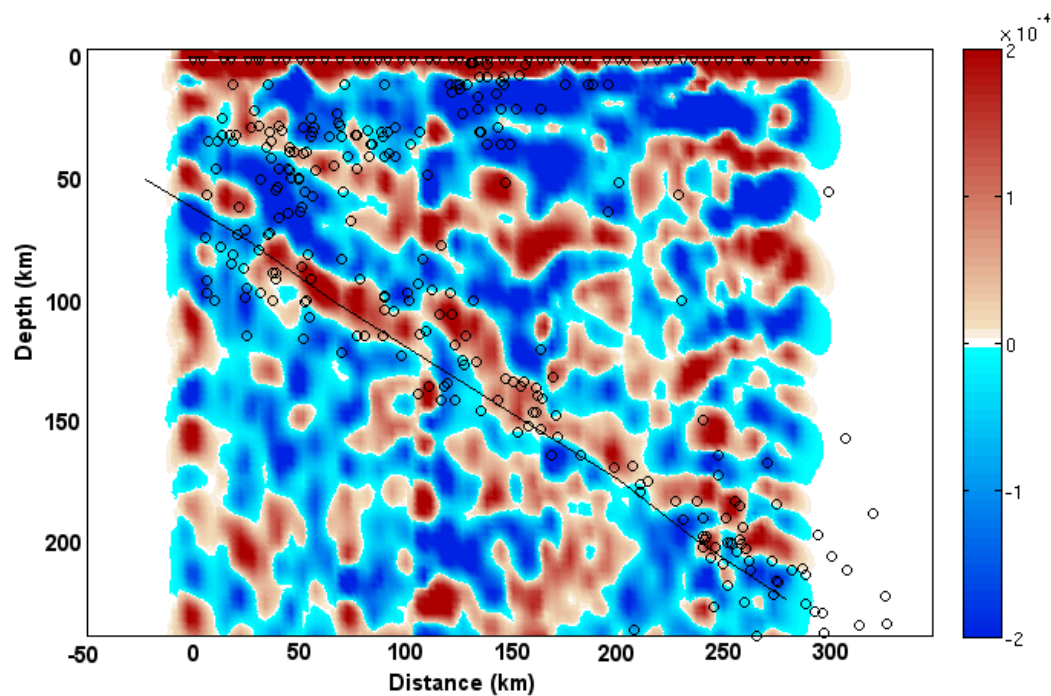

Figure 4.24: Receiver function plot for Line 1 plotting common conversion point (CCP) stacks at each bin distance as a function of depth.

4.7 Finite Difference Modeling

Several related finite difference codes were used for various modeling purposes. The main code used is the same employed in Kim et al, 2010 is a staggered grid finite-

difference solution of the linear elastic 2D wave equation. The principle variables are (U,W) which are the (x,z)-components of (particle) velocity, T_{xx} and T_{zz} which are normal stresses, T_{xz} which are shear stresses, λ the Lame coefficient, μ the other Lame coefficient or shear modulus, $\gamma=\lambda+2\mu$, and B which is the buoyancy which is 1/density. The stress updates are done according to the equations:

T_{xx} += $dt*(\gamma*U_x+\lambda*W_z)$,

T_{zz} += $dt*(\lambda*U_x+\gamma*W_z)$,

T_{xz} += $dt*\mu*(U_z+W_x)$.

The velocity updates are done according to the equations:

U += $dt*B*(T_{xx,x}+T_{xz,x})$,

W+=$dt*B*(T_{xz,z}+T_{zz,z})$,

where dt is the time step.

The inputs to the code are the P wave velocity model, the model and source parameters, and a list of ray parameters. The finite difference code models the propagation of a P plane wave at a given ray parameter from a direction set usually as the lower left or right corners of the model. The resultant synthetic seismograms are deconvolved using iterative time domain deconvolution to produce synthetic receiver functions which can be compared to data. Examples of the models and synthetics can be seen in figures 2.10, 3.3, 3.8, and 3.11.

Structural and velocity models derived from receiver function observations and testing using the aforementioned finite difference code can then be used to model the wave propagation from local events near the arrays to produce synthetic seismograms which

can be compared with local data. The 2D finite difference code was described by

Vidale et al, 1985 and used in Chen et al, 2007. The P-SV and SH systems are modeled

separately for each model.

As described in Chen et al. (2007),

"The scheme for generating point source seismograms for shear dislocations using 2-D numerical methods is discussed by Helmberger and Vidale [1988]. It is based on expanding the complete 3-D solution in asymptotic form and separating the motions into the SH and P-SV systems. This analytical Cagniard-de-Hoop method is used to derive closed form expressions appropriate for 2-D FDM source excitations. Synthetics generated by this method are bench-marked in the above mentioned study."

Examples of models and synthetics using this code can be seen in figure 2.12.

Table 4.1
Largest local events since start of arrays, NEIC locations

Date	Lat/Lon	Depth	Mag
10/28/2011	-14.44/-75.97	24	6.9
11/13/2009	-19.39/-70.32	27	6.5
01/30/2012	-14.17/-75.64	43	6.4
03/06/2011	-18.02/-69.36	118	6.3
05/14/2012	-17.68/-69.59	105	6.2
05/06/2010	-18.06/-70.55	37	6.2
07/08/2008	-15.99/-71.75	123	6.2
06/07/2012	-15.88/-72.41	110	6.1
05/23/2010	-13.93/-74.35	101	6.1
07/12/2009	-15.04/-70.44	198	6.1
04/17/2009	-19.58/-70.48	25	6.1
02/02/2009	-13.58/-76.56	21	6
06/08/2011	-17.08/-69.52	145	5.9
04/02/2011	-19.58/-69.07	84	5.9
09/13/2010	-14.61/-70.78	179	5.9
09/30/2009	-15.55/-69.29	255	5.9
04/05/2010	-19.86/-68.84	94	5.8
09/05/2009	-15.12/-70.25	210	5.8
05/18/2009	-15.66/-74.84	22	5.8
07/02/2012	-14.42/-75.6	39	5.7
09/22/2010	-13.39/-76.07	50	5.7
03/15/2009	-14.45/-70.36	189	5.7
05/06/2012	-13.82/-75.8	54	5.6
10/28/2011	-14.51/-75.84	10	5.6
10/28/2011	-14.38/-76	22	5.6
12/24/2009	-15.77/-73.98	59	5.6
01/31/2009	-19.41/-69.07	102	5.5

4.8 Local Events and Future Study

The seismic arrays are located in a region with a significant amount of seismicity which can provide another valuable source of information about the structure of southern Peru besides teleseismic receiver functions. Some of the largest events closest to the array are listed in table 4.1 and are plotted in figure 4.25. The locations are from the National Earthquake Information Center (NEIC). The locations were checked during the analysis, and while some NEIC locations seemed to work reasonably well from the accuracy of P and S picks, in general there was some locational error, and locations posted on the website of the Instituto Geofisico del Peru (IGP) were found to work better in those cases.
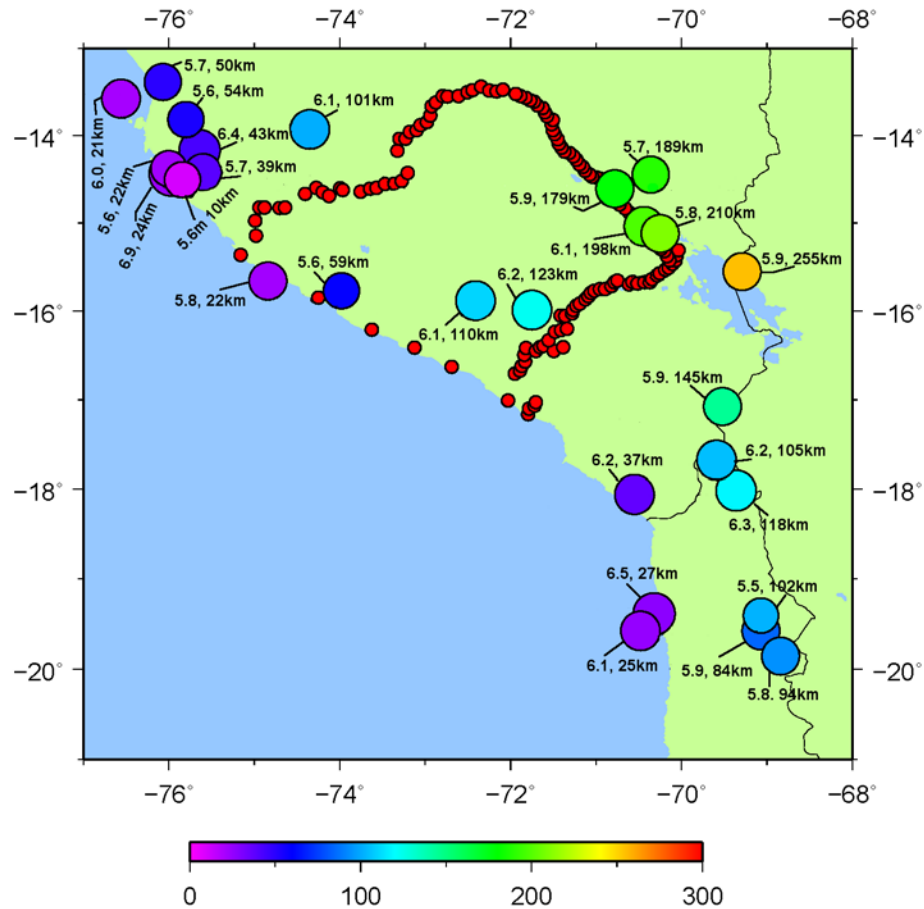
Figure 4.25: Map of largest events in the immediate vicinity of the arrays during the time the arrays were operating. More information about these events is found in the table 4.1. The magnitude and depth are labeled and color corresponds to depth in kilometers. Locations are from the NEIC earthquake catalog.

Several of the large, deep events near Juliaca were of interest for modeling. Events which were particularly focused on include the earthquakes on 7/12/2009 (Mw 6.1, 198 km depth), 9/5/2009 (Mw 5.8, 210 km depth), and on 9/30/2009 (Mw 5.9, 255 km depth). Deep earthquakes near the array were used to make local receiver functions which can provide more detailed information about the Moho and midcrustal structure. Other methods analyzing local events include looking for the precursor to the pP arrival

from reflections off of the Moho as detected by teleseismic stations which provides a

possible check for Moho depths calculated by receiver function methods. Velocity

models and features observed in local data can also be checked using finite difference
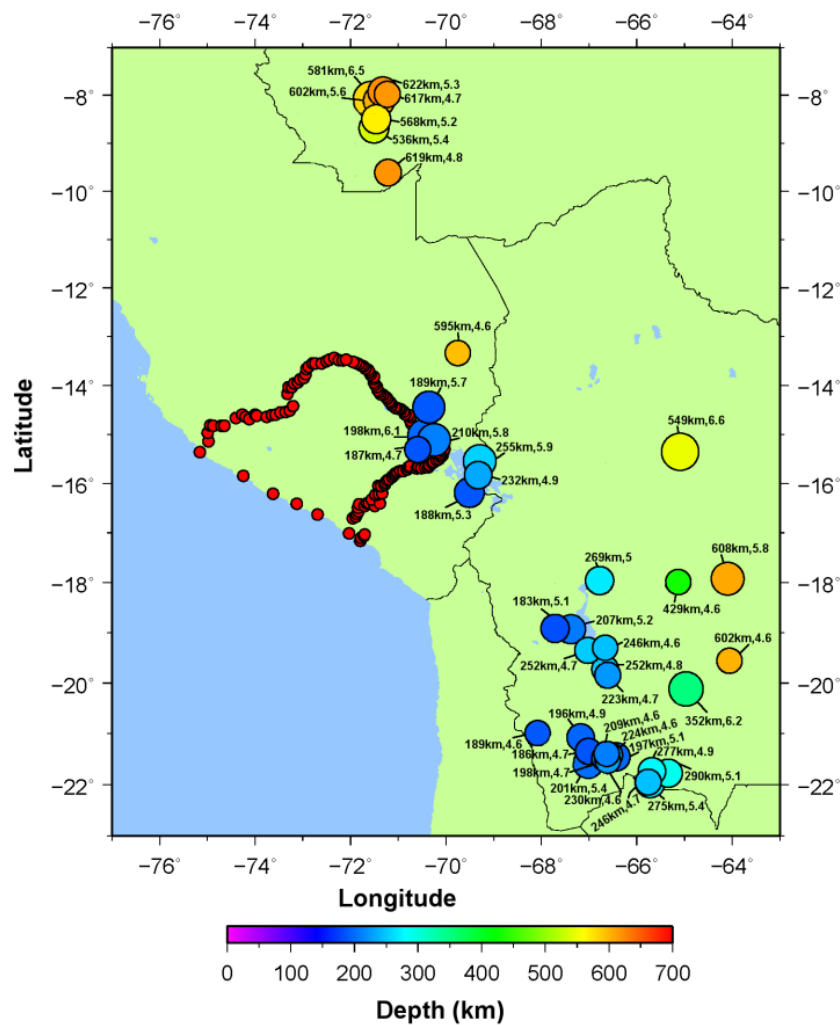
modeling.

Figure 4.26: Events deeper than 180 km which can be used for local receiver function analysis as provided by the NEIC earthquake catalog.

4.8.1. Local Receiver Functions

Local events were also used to make receiver functions. Due to the thick crust

beneath the Altiplano, events were only selected if they were deeper than 180 km and

close to the arrays to avoid interference with crust not directly beneath the station. The

locations of the largest and closest events meeting the depth criteria are shown in

Figure 4.26. By picking very high quality local events which are almost directly

beneath the stations, it is possible to probe the crustal structure in more finer detail than

is possible with teleseismic events as discussed in Calkins et al. (2006) where events

with corner frequencies up to 2.5 or 5 Hz were used to better define crustal interfaces

which were not well-defined by teleseismic energy. However dealing with higher

frequencies also results in more high-frequency noise. An advantage of this method for

southern Peru would to better define the extent of the midcrustal structure whose

western boundary is not well defined by teleseismic receiver functions. A sample local

event is an event on 11/22/2011 which was a magnitude 6.6 earthquake at a depth of

549km located due east of Juliaca about 550 km away from the closest stations. An

example of the receiver function and data quality can be seen in figure 4.27. This event

was detected by all arrays. The resultant receiver function images are clearest for the

closest array, Line 1, which is shown in figure 4.28 for a corner frequency of 0.5Hz. At

this depth and distance, a clear slab image is not expected, however the Moho and

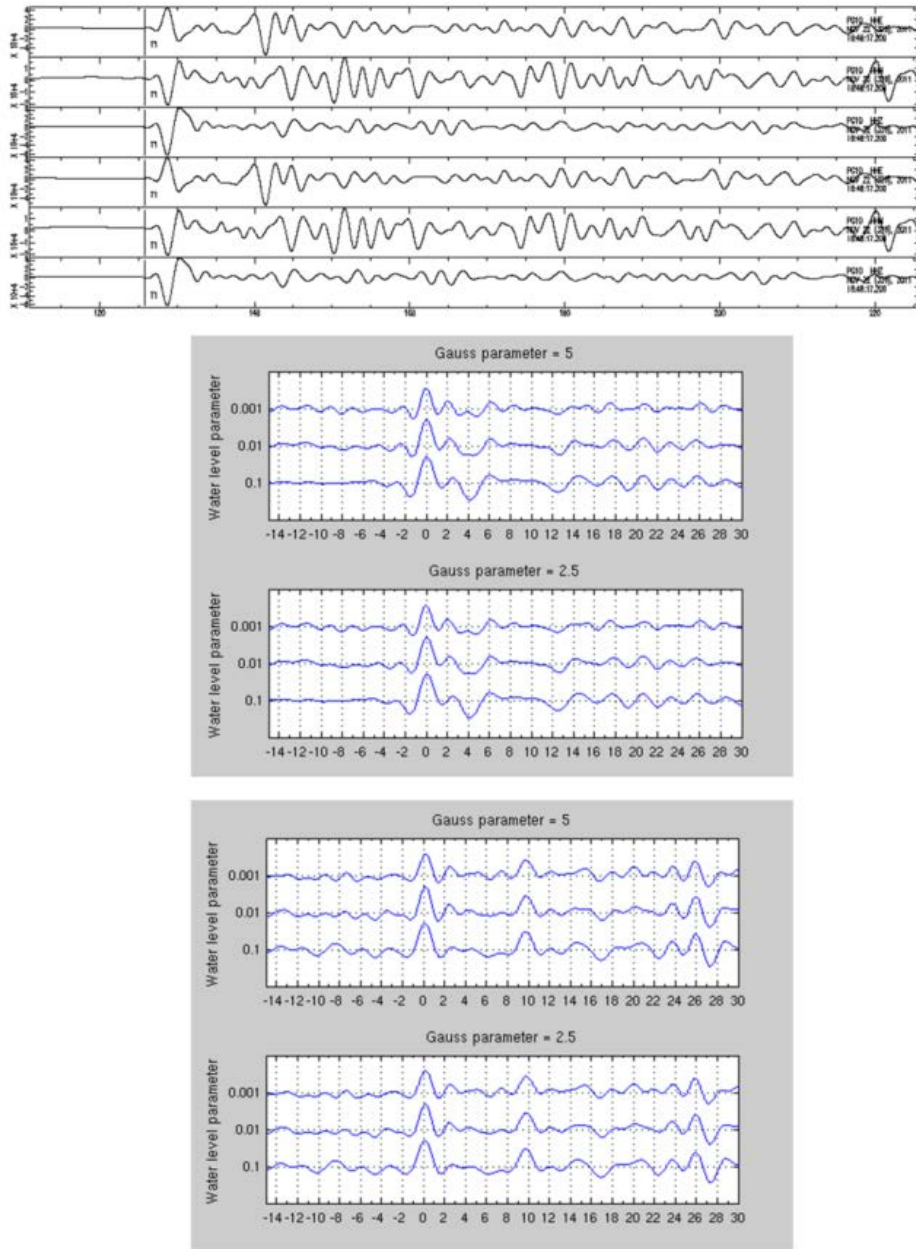midcrustal structure are very well resolved.

Figure 4.27: Local receiver function analysis for the deep local event on 11/22/2011 (magnitude 6.6 at 549 km depth located due east of Juliaca). Top shows data quality and bottom panel shows receiver function quality.
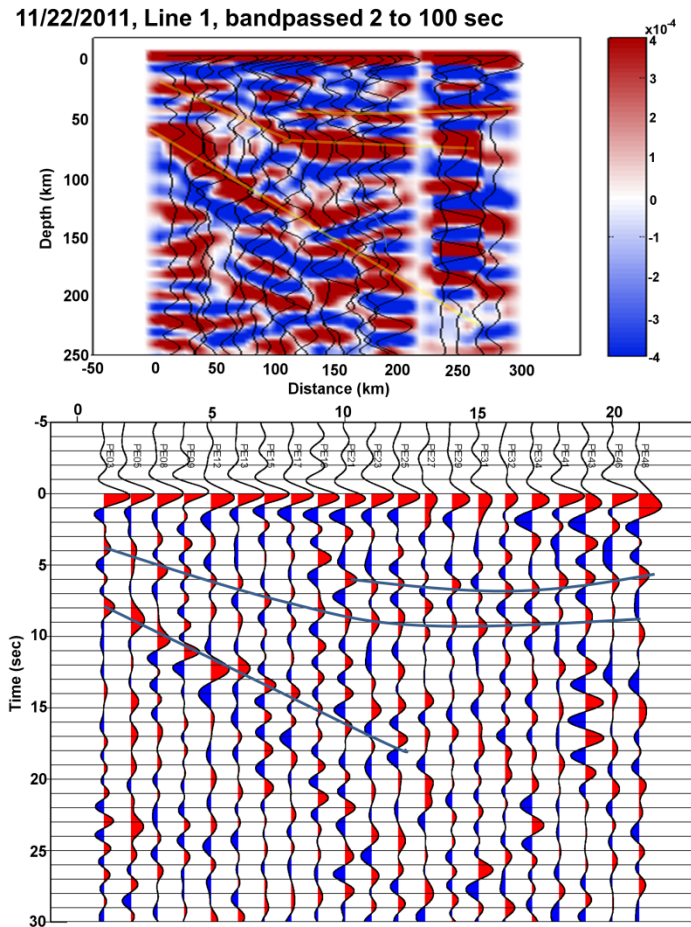
Figure 4.28: Line 1 image based on receiver functions from a 549 km deep local event on 11/22/2011 bandpassed to 2 seconds located due east of Juliaca.

After the quality test at a bandpass frequency of 2 seconds, the receiver functions were

also checked at higher frequencies up to a corner frequency of 2 Hz to find out if

smaller scale features could be resolvable. The results for 2 Hz are shown in figure

4.29. From the comparison of figures 4.28 and 4.29, although the results are consistent,

it appears that increasing the frequency increases noise with no noticeable

improvements in resolution. Therefore it appears that the corner frequencies used for

the analysis of teleseismic events are also the most appropriate for local events.
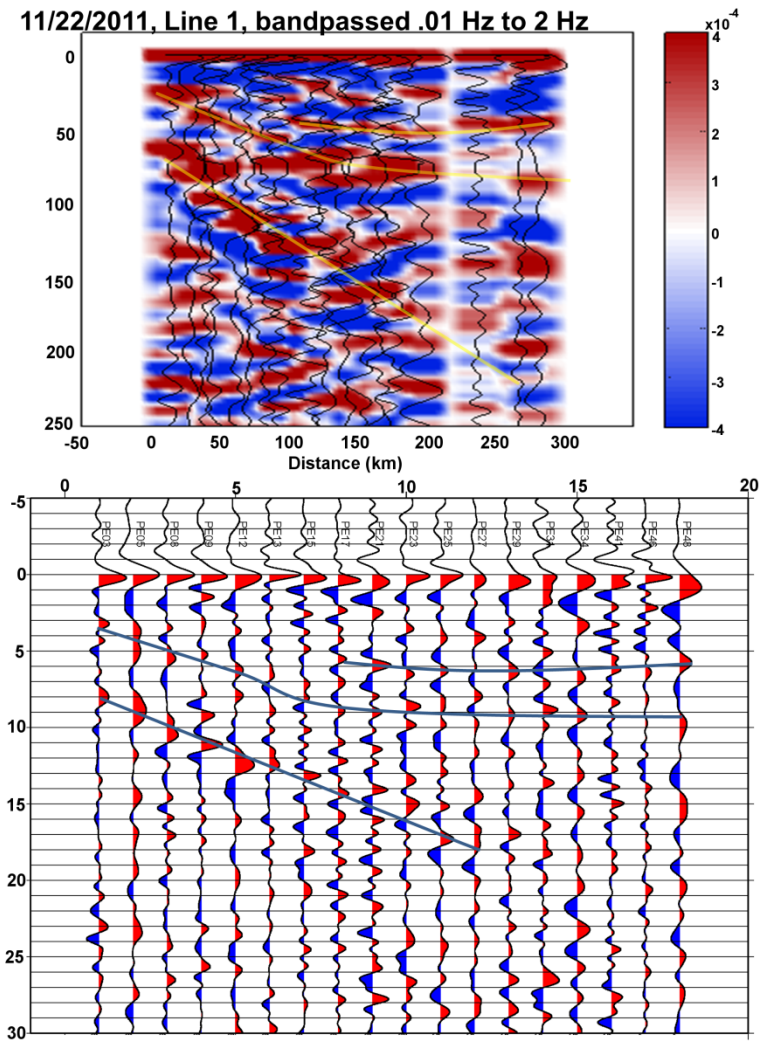

Figure 4.29: Line 1 image based on receiver functions from local event on 11/22/2011 bandpassed to 2 Hz. Compare with the same image for in figure 4.28 bandpassed to a lower frequency.

4.8.2. Precursors to pP or sS

Estimations for crustal thickness can be obtained by looking for precursors to the pP or

sS phase from Moho underside reflections, pmP or smS, using deep-focus earthquakes

(McGlashan et al, 2008; Schenk et al, 1989; Zhang & Lay, 1993; Zheng & Lay, 2006).

Following McGlashan el al (2008), crustal thickness can be estimated between the

delay time between the pP phase and pmP phase using the formula

$$t_{pP} - t_{pmP} \approx 2h\sqrt{V_{Pc}^{-2} - p^2},$$

where h is the crustal thickness, V_{Pc} is the P wave velocity, and p is the ray parameter

(assumed to be the same for the pP phase and pmP phase). Due to the deep crustal

thickness in the Altiplano, only events with magnitude greater than 6.0 with a depth

greater than 100 km were considered. The location of events which were analyzed

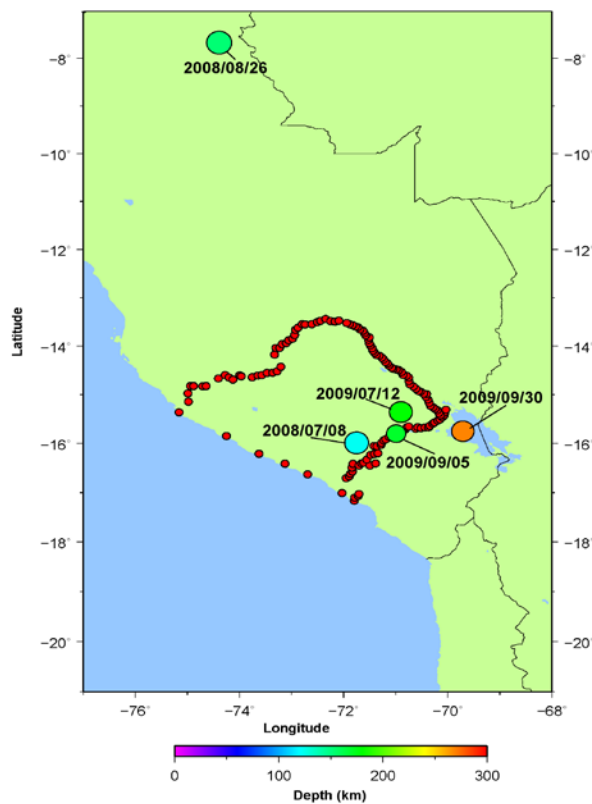using this method are shown in figure 4.30.

Figure 4.30: Map of specific local events analyzed for underside Moho reflections (precursors to pP and sS). Events in 2009 have locations from the IGP (Instituto Geofisico del Peru) while the 2008 events are as located by the NEIC.

Both pP precursors and sS precursors were checked for. Data from the stations in Southern California (the CI array) which detected the teleseismic Peruvian events and had a good signal-to-noise ratio were utilized to check for underside reflections from the Moho. Selected stations were aligned by the P (or S arrival for the sS phase) and then stacked. The precursors are expected to be a very small signal and are generally hard to detect in individual stations so stacking is used to minimize noise and bring out a small signal which consistently appears on a majority of stations. Results were found to be better if the data was bandpassed to longer periods such as a 2 second corner frequency. Major arrivals such as P, pP, S, and sS were generally very clear for all events. Timings for those and other nearby phases were checked using a TauP seismic travel time utility based on IASP91. Where locations from IGP (Instituto Geofisico del Peru) were available, they were used instead of NEIC because analysis of data collected by the Peruvian arrays showed that the IGP locations generally resulted in better P and S picks (thus the events in 2009 shown in figure 4.30 are all IGP locations , depths, and magnitudes). Using estimates of Moho depth from receiver functions (where applicable), it is possible to estimate the expected location of the precursor and compare with the stacks.

131
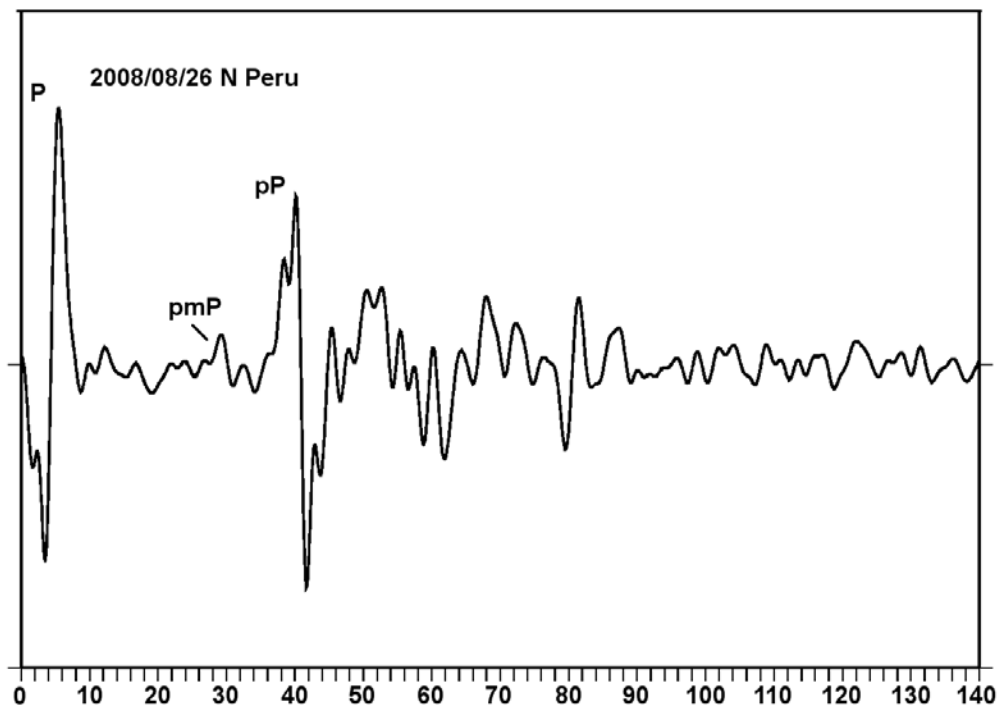
Figure 4.31: Stack of teleseismic data collected from Southern California stations recording an earthquake in northern Peru on 8/26/2008 showing possible precursor to pP from underside Moho reflection (see map in figure 4.30).

Figure 4.31 shows a stack from a magnitude 6.3 earthquake in Northern Peru from Aug.

26, 2008. The largest signal between the P and pP arrival appears to be the precursor

due to underside reflection off of the Moho. Although no receiver function data is

available in this region, a look at the location and topography of the area (see figure

1.1) shows that this location is most likely at lower elevations in the Subandes where

the Moho depth is shallower. The Moho depth appears to be around 40 km depth

which is around the average for that region (Lloyd et al, 2010; Assumpçao, 2012). The

longer period S wave results in which precursors to the sS phase are indicative of

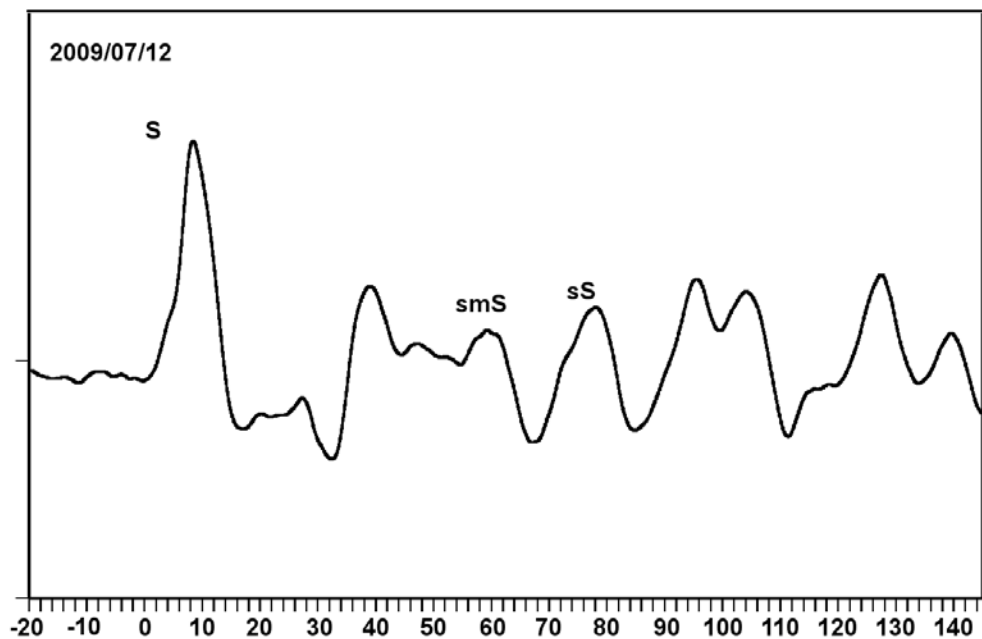underside reflections from the Moho are down in figure 4.32.

Figure 4.32: Stack of teleseismic data for 2009/07/12 showing S wave signal and possible precursor to sS from underside Moho reflections (see location in figure 4.30).

In this figure, the sS phase appears small relative to the pP phase and can be identified by the timing of phase arrivals. An earlier phase which may be the smS phase is consistent with a Moho depth of 70-75 km which is what is observed with receiver functions beneath that region of the Altiplano. Some other results for the pP phase are shown in figure 4.33 where the Moho depth is expected to be similar to the depth in figure 4.32 (aside from the Arequipa earthquake were the Moho depth is closer to 60 km depth from receiver functions).
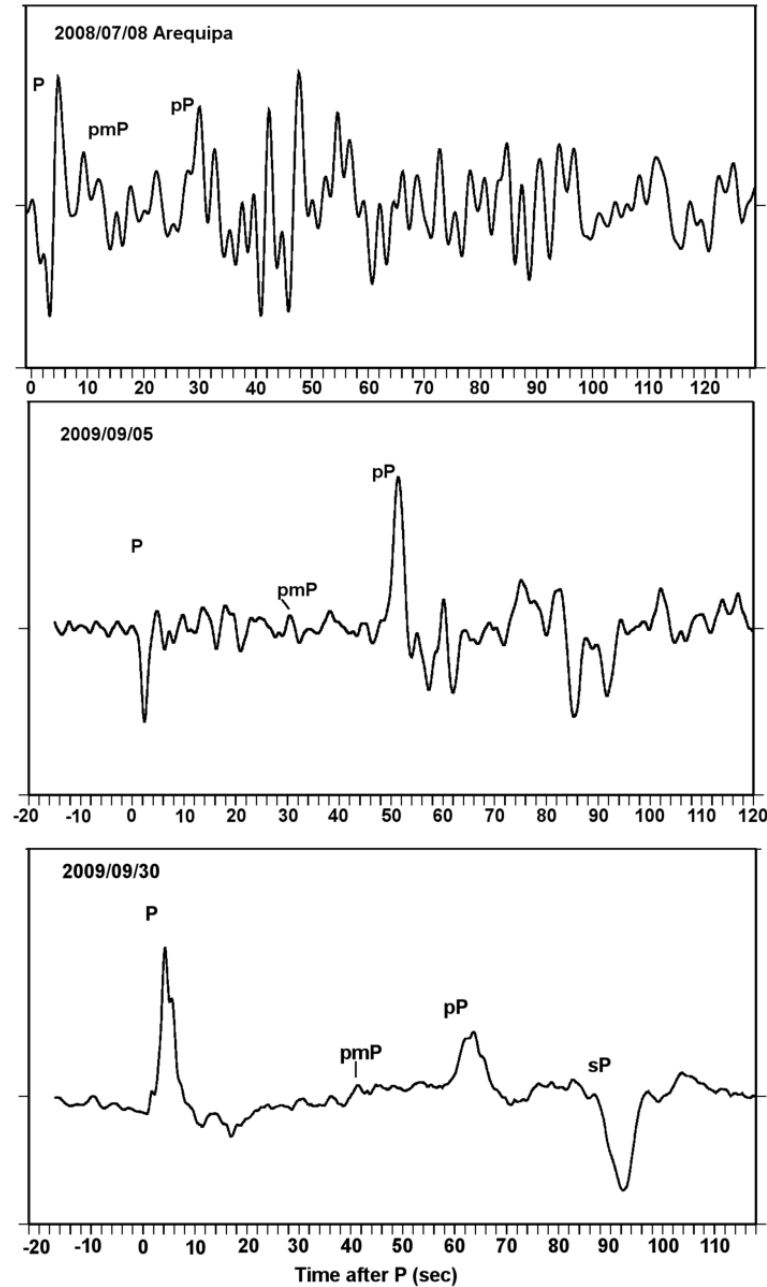
Figure 4.33: Stacks from Southern California recordings of Peruvian earthquake which occurred on 2008/07/08, 2009/09/05, and 2009/9/30 for looking for pP precursors. Locations are given in figure 4.30 and earthquake details in table 4.1.

However the pmP phase appears to be so small that it is generally hard to identify over

the surrounding noise without prior knowledge of the Moho depth and phase timing

estimations. Thus in these cases very careful selection of only the highest quality

teleseismic data and careful stacking is needed for precursor identification. In some

cases the precursors may be visible for individual stations.

4.8.3. Modeling Local Events

Figure 4.34. Vertical component seismogram traces for Line 1 showing data from event
on 7/12/2009 bandpassed to 1 second (top) and 10 seconds (bottom).

Local earthquake data from large, deep events recorded by the seismic array

(particularly on 7/12/2009, 9/5/2009, and 9/30/2009) was analyzed with locations as

shown in figure 4.30. The three events were recorded by Line 1 located in the normal

subduction region and the vertical components of the seismogram are shown in figures
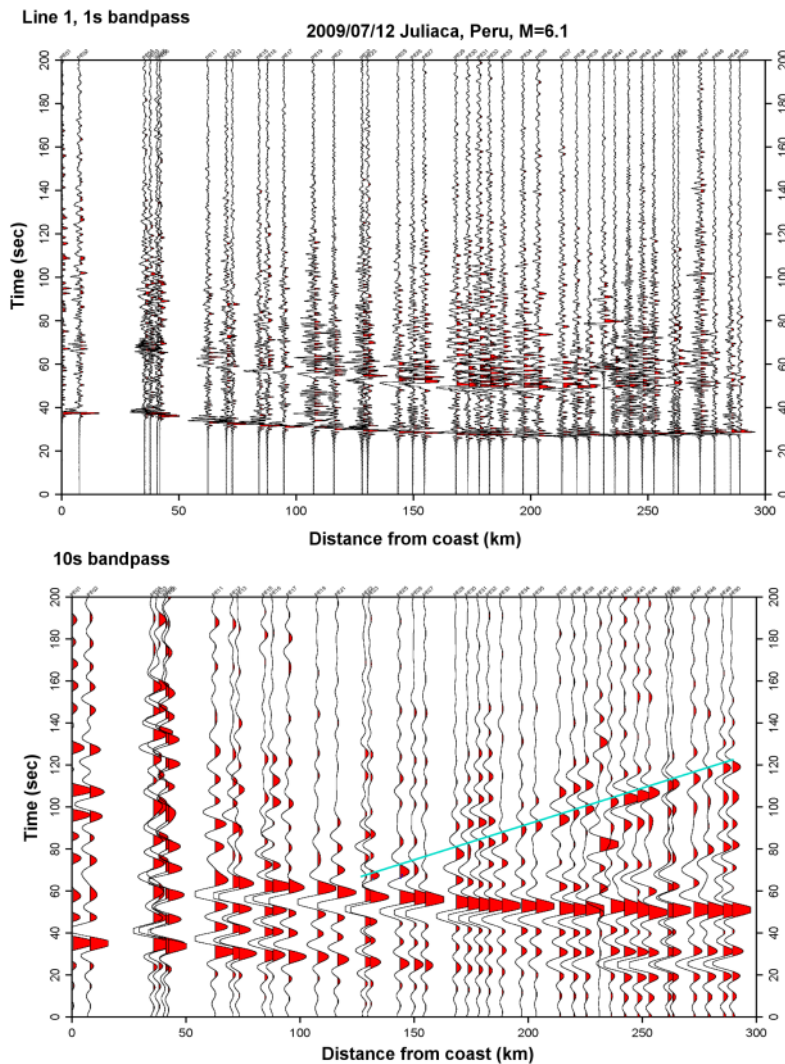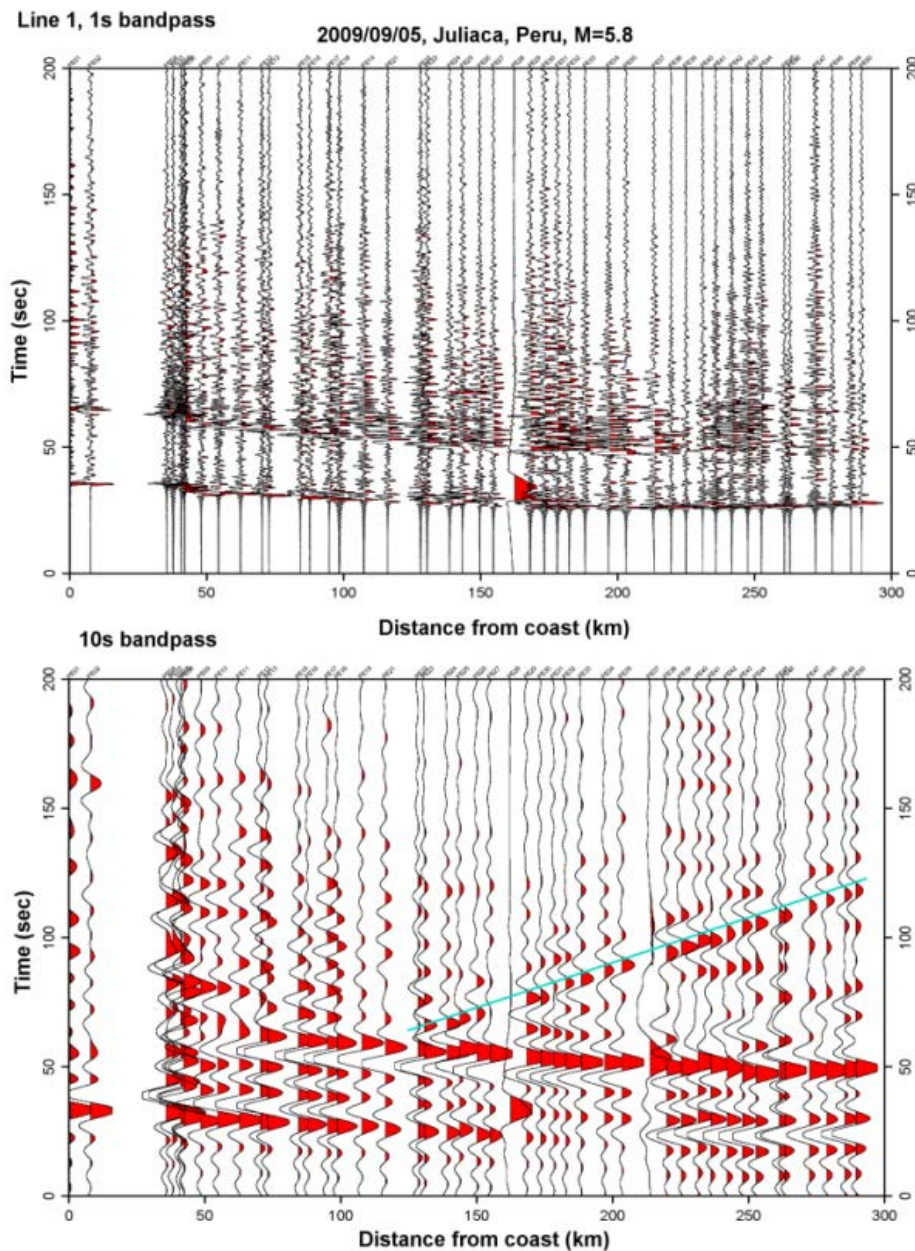
4.34-4.36.

Figure 4.35 Vertical component seismogram traces for Line 1 showing data from event
on 09/05/2009 bandpassed to 1 second (top) and 10 seconds (bottom)
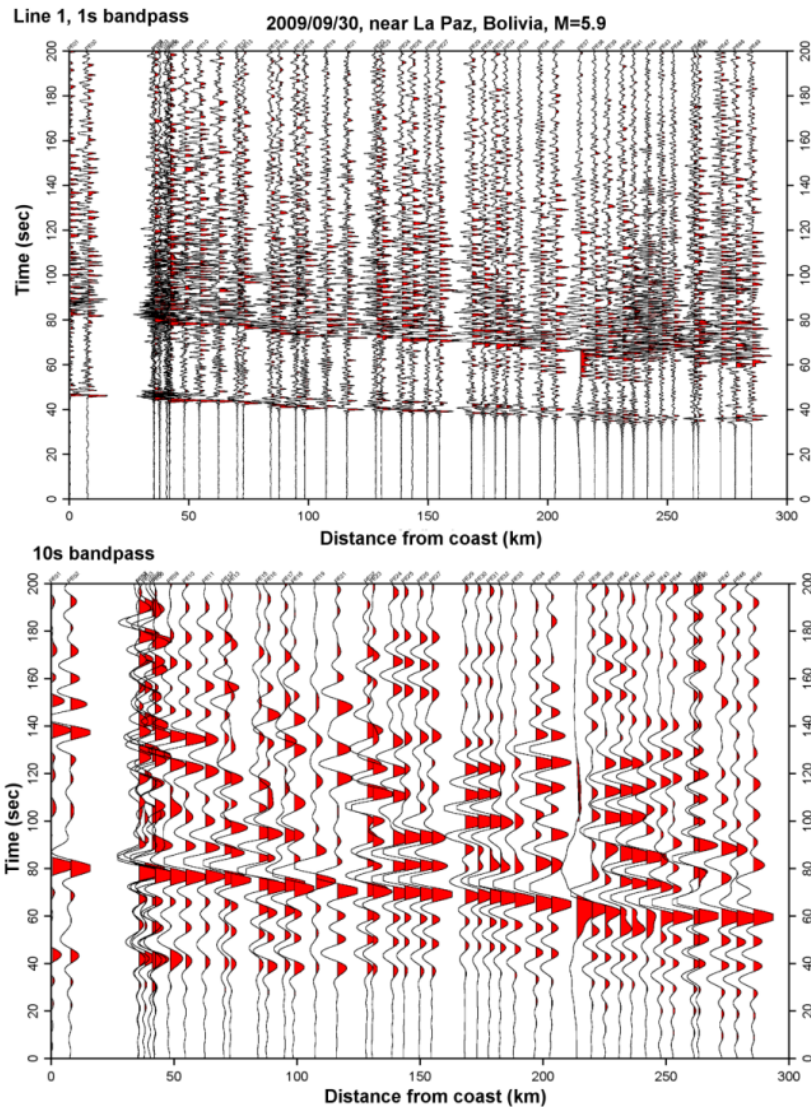
Figure 4.36. Vertical component seismogram traces for Line 1 showing data from event on 09/30/2009 bandpassed to 1 second (top) and 10 seconds (bottom).

The top portion of each figure shows the data bandpassed to 1 second while the bottom portion shows the same data bandpassed to 10 seconds. The major arrivals from the S and P wave are visible in each plot. An observation that was made was that there appeared to be a signal originating from near the center of the array which appeared to be a reflection. The signal is only visible in the longer period band-passed data

indicating that the signal may originate from some kind of surface wave reflecting off something in the subduction system (see blue lines in figure 4.34 and figure 4.35). Although the signal appears in multiple local events, the signal is not obvious for the event on 2009/09/30 shown in figure 4.36 indicating a possible azimuthal dependence on the direction of the reflector. Several models were tested to determine if a structural model could be used to explain the possible origin of the observed signal as shown in figure 4.37.
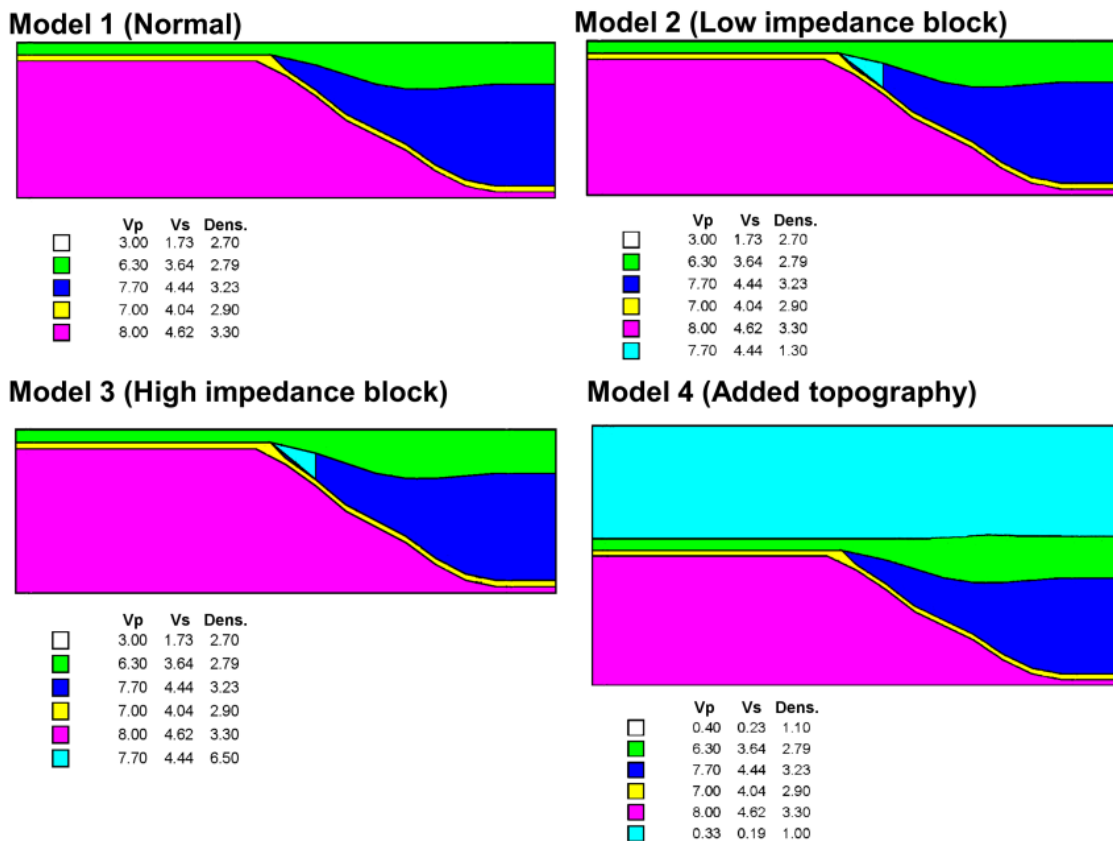
Figure 4.37: Possible models for analyzing the local events shown in figures 4.34-4.36 using finite difference code. The normal model consists of a homogeneous crust with an average crustal velocity, the mantle wedge, subducting oceanic crust, and underlying mantle with average velocities. The Low impedance and high impedance models contain a wedge with differing density in the corner of the mantle wedge to study whether reflections from the corner of the subduction zone could cause

reflections similar to those observed in local data (see figures 4.34-4.35). The fouth model is similar to model 1 but has added station topography. The light blue color has properties of air.

One possibility was that the signal was derived from a reflection off the corner of the subduction zone near where the asthenospheric wedge is cut off by the Nazca plate as it subducts near the oceanic trench. To test this model, a small wedge was inserted in the corner of the subduction zone with a different impedance (either higher or lower) to cause rays to reflect off. The impedance contrast was given a density very different from the surrounding materials to encourage reflections for the purpose of generating a signal which could then be compared with observations in the data. Another possibility was that the signal could be related to reflections off of topography. These cases were compared to a simple model of the subduction zone consistent with the model in figure 2.10A. To simplify the resulting signals, no midcrustal structure was included in these models.
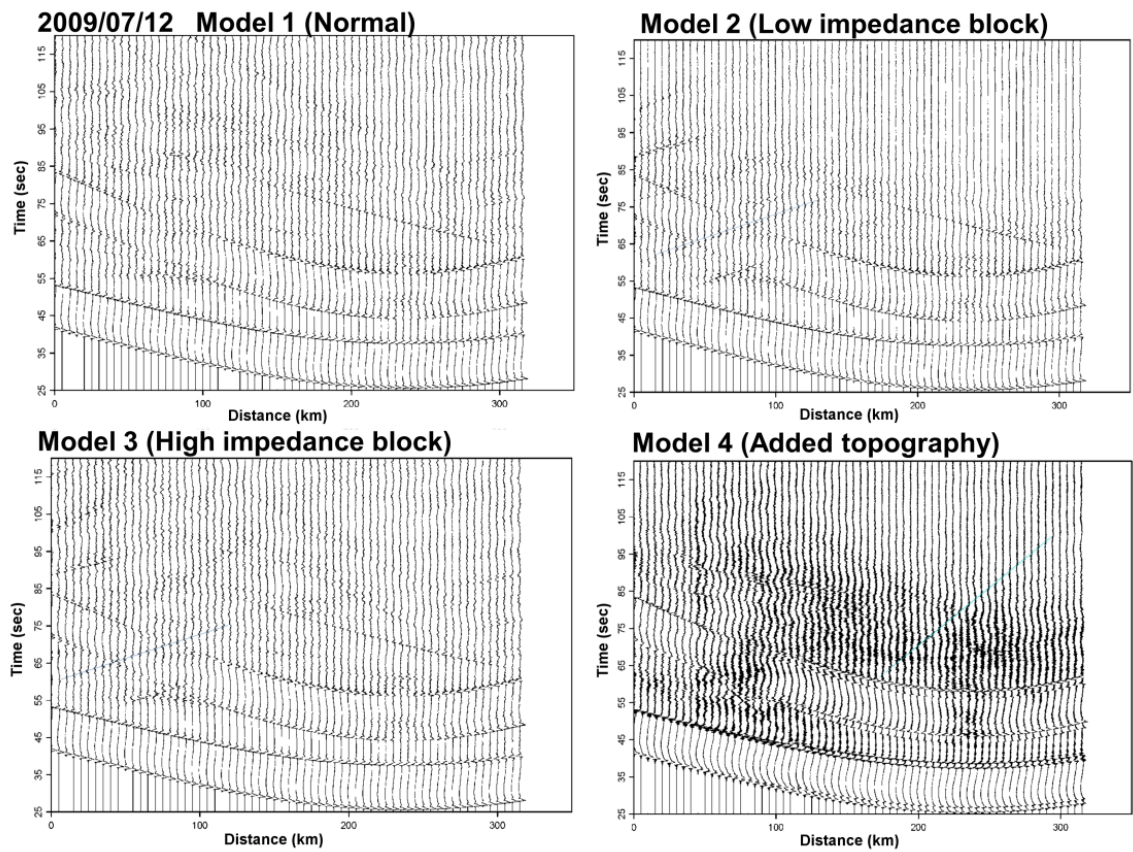
Figure 4.38 Finite difference synthetics for 2009/07/12 based on the models in figure 4.37.
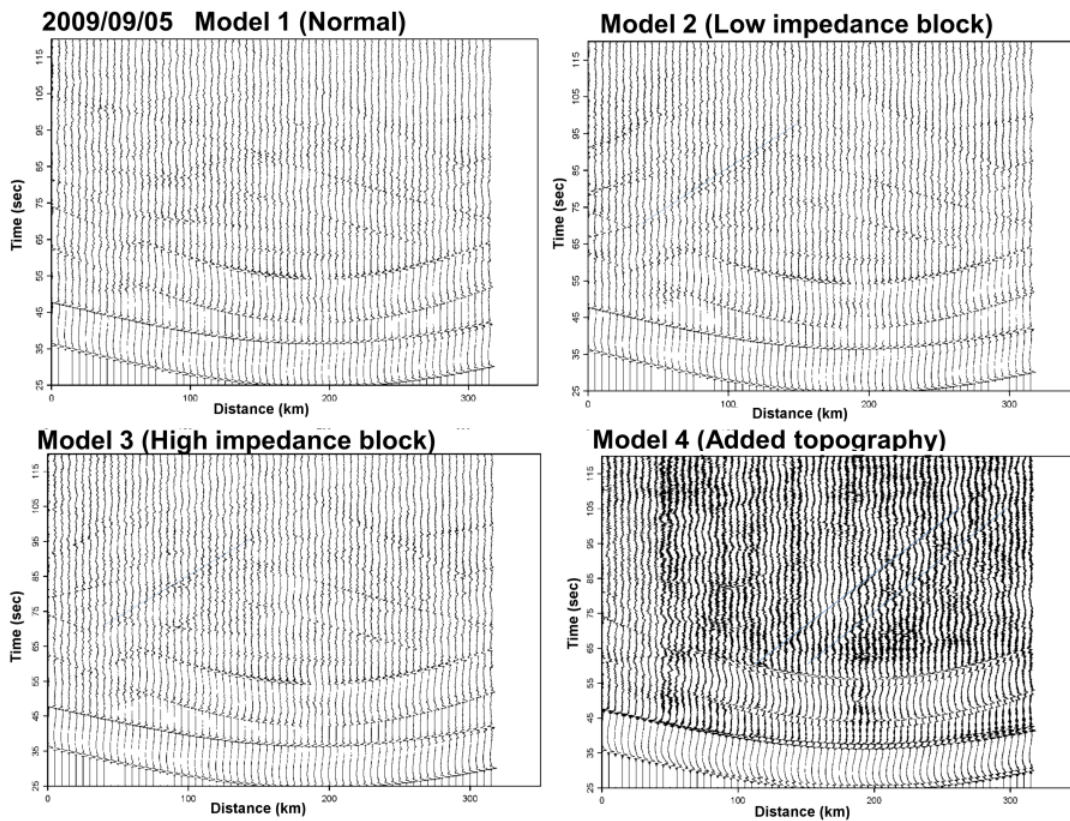
Figure 4.39 Finite difference synthetics for 2009/09/05 based on the models in figure 4.37.
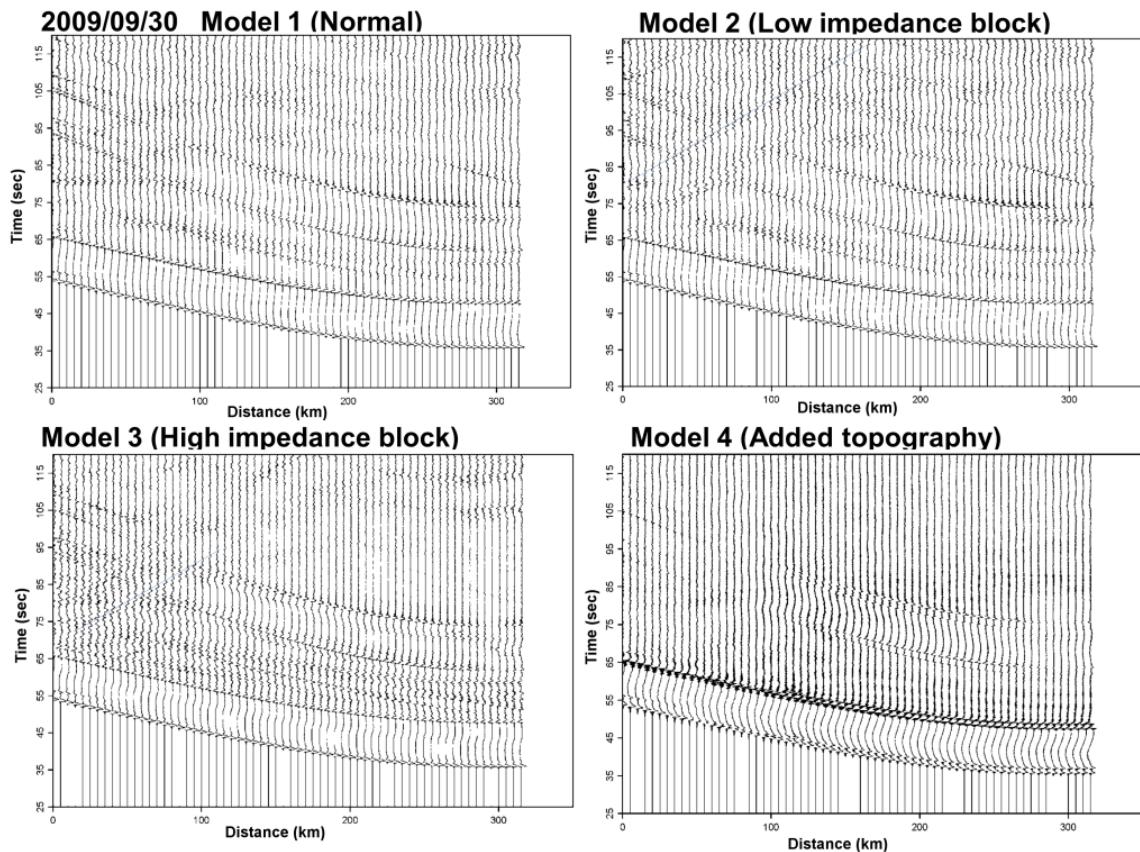
Figure 4.40 Finite difference synthetics for 2009/09/30 based on the models in figure 4.37.

Synthetic seismograms generated from finite difference modeling are shown in figures 4.38–4.40 for each of the three events for the models shown in figure 4.37. No reflections in the direction observed in the 10 second bandpassed data (figures 4.34-4.35) can be seen in the first normal model (model 1 in figure 4.37). For the case where there is an impedance contrast at the corner of the subduction zone, a few reflections are observed but the reflectors originate near the start of the model (for example see some reflections starting at about 60 seconds at zero distance in figure 4.38, or ~55 seconds in figure 4.39, or ~80 seconds in figure 4.40). However the synthetics

corresponding to the model including topography in figure 4.38 and 4.39 shows a small

amplitude signal originating from the same approximate location as in the data and

traveling in the same direction.   Similar to the data, the signal is not obvious in the

topography model for the event on 9/30/2009. Although there are other possible

explanations for the signal observed in the 10 second local data besides reflections off

topography, the use of finite difference modeling to investigate several possible cases

shows that it is possible for a structural model to provide a possible fit to the observed

data.

4.8.4. Future Work: Determination of EQ Loc. and Focal Mechanisms.

The cut and paste code (CAP) was used to check earthquake focal mechanisms (Zhao

& Helmberger, 1994; Zhu & Helmberger, 1996). Two different crustal models were

tested for making Greens Functions. One model was modified from Ocola et al, 1995

(Somerville et al, 2008) which is based on geophysical studies along the southern Peru

coast. The model is shown in table 4.2. The other model tested used the Vp, Vs, and

density from IASP91 for the upper 250 km and tested lower values for the attenuation

(Qp and Qs). Attenuation studies from the Peru/Chile or Central Andean regions

(Baumont et al, 1999; Sumner, 1967; Whitman et al, 1992) found significant variation

in Q values. Previous values for the Altiplano based on results from the BANJO and

SEDA array (modified from Myers et al, 1998) found values for the crust in the

Altiplan o of Vp~6.2, Vs~3.6, Qp~500, and Qs~100. For the Altiplano asthenosphere

the values found were Vp~8.3, Vs~4.6, Qp~500, and Qs~200 (Heit, 2005).

CAP code was used to analyze a magnitude 6.9 earthquake on 10/28/2011 which occurred just north of Line 3 and found a focal mechanism similar to the Harvard CMT solution (see figure 4.41) after searching the full range of strike, dip, and rake but fits between data and synthetics were poor. More work with this method is needed to produce good focal mechanisms.
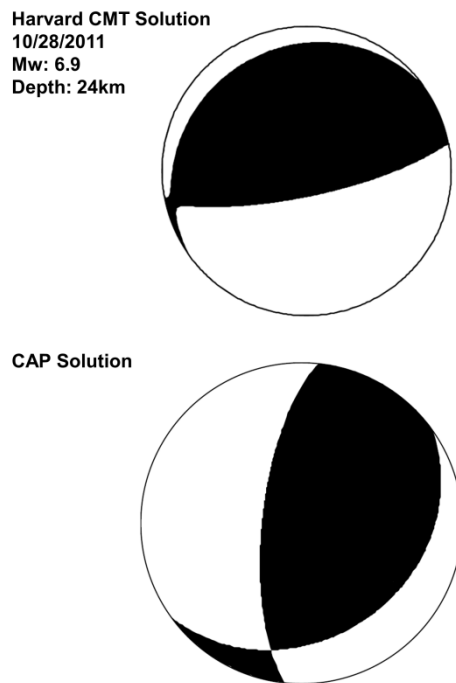
Figure 4.2 CMT solutions for 10/28/2011.

Table 4.2 Crustal model for S. Peru, from Ocola et al, 1995					
Thickness	Vp	Vs	Density	Qp	Qs
6.7	5.3	3.03	2.1	2000	900
4.6	6	3.37	2.5	2000	900
18.1	6.5	3.65	2.78	2000	900
15.8	7.3	4.1	3.18	2000	900
16	8.1	4.5	3.4	2000	900
100	8.101	4.501	3.401	2000	900

4.9 Summary and Conclusions

The previous chapters present receiver function results from three seismic arrays in Southern Peru. A total of about 100 broadband stations were deployed over the course of several years between 2008 and 2011, providing dense station coverage along the arrays and a valuable data set for the analysis of both local and teleseismic earthquakes. Teleseismic receiver functions were formed using P, PP, PKP, S and SKS phases and both frequency and time domain deconvolution methods were used. Resulting images using backprojection, CCP stacking, or migration provide high quality images of the subduction system. The areas imaged include the region of normal subduction where the Nazca plate dips at about a 30 degree angle, the transition from normal to flat slab subduction suggested to be a contortion rather than a tear in the slab, and the flat slab region near the subduction of the Nazca Ridge. In addition to clarifying the shape of the slab, the Moho depth was observed to reach a maximum depth of about 70-75 km beneath the Altiplano. Receiver function images also show a positive impedance midcrustal signal at 40 km indicating a velocity increase which is suggested to be a possible observation of the underthrusting Brazilian Shield. Crustal signals which are less defined in teleseismic receiver functions can be clarified by looking at local receiver functions from deep events close to the arrays. Receiver functions for individual stations can be stacked to obtain estimates of Moho depth and Vp/Vs ratio. The average Vp/Vs ratio for the region was found to be around 1.75 with a few regions of elevated Vp/Vs near the active volcanic arc. The Moho depths obtained from

receiver function images can be confirmed through other methods such as looking for

precursors to the pP and sS phases in teleseismic recordings of local Peru events. The

precursors, if observed, come from underside Moho reflections and can be used to

estimate crustal thickness. Although most of the receiver function results come from an

analysis of radial receiver functions, a look at energy on transverse receiver functions

can provide information about dipping structure or anisotropy. Observations from Line

2 in the transition from normal to flat slab subduction suggest that the area has some

anisotropy with a symmetry axis in possibly an ~E/W direction. This anisotropy might

provide an explanation for differences between images using data from different

azimuthal directions (e.g., comparing images from northerly directions with southerly

directions). Simple structural and velocity models can be tested using finite difference

methods to produce synthetic receiver functions or model local events.

These results provide valuable new information about the structure of the subduction

zone in southern Peru where the subduction transitions from shallow subduction in

central Peru to steep subduction in southern Peru.

Chapter 4 References

· Assumpçao, M., M. Feng, A. Tassara, J. Julià (2012), Developing Models of Crustal
   Thickness for South America from Receiver Functions and Surface Wave
   Tomography, *Tectonophysics*, in review/press.

· Baumont, D., A. Paul, S. Beck, and G. Zandt (1999), Strong crustal heterogeneity in
   the Bolivian Altiplano as suggested by attenuation of Lg waves, *J. of Geophys. Res*.,
   104 (B9), 20,287- 20,305.

· Burdick, L.J. and D.V. Helmberger (1974), Time functions appropriate for deep
   earthquakes, *Bull. Seismol. Soc. Amer*., 64, 1419-1428.

· Calkins, J. A., G. Zandt, H. J Gilbert, and S. L. Beck (2006), Crustal images from San
   Juan, Argentina, obtained using high frequency local event receiver functions,
   Geophys. Res. Lett., 33, L07309.

· Chen, M., J. Tromp, D. Helmberger, H. Kanamori (2007), Waveform modeling of the
   slab beneath Japan, *J. Geophys. Res*., 112, B02305.

· Cunningham, P., and S. Roecker (1986), Three-dimensional P and S Wave Velocity
   Structures of Southern Peru and Their Tectonic Implications, *J. of Geophys.
   Res.*, 91 (B9), 9517–9532.

· Endrun, B., T. Meier, M. Bischoff and H.-P. Harjes (2004), Lithospheric structure in
   the area of Crete constrained by receiver functions and dispersion analysis of
   Rayleigh phase velocities, *Geophys. J. Int*., 158, 592-608.

· Frassetto, A., G. Zandt, H. Gilbert, T.J. Owens and C.H. Jones (2010), Improved
   imaging with phase-weighted common conversion point stacks of receiver functions,
   Geophys. J. Int, 182, 368-374.

· Geissler, W., F. Sodoudi, and R. Kind (2010), Thickness of the central and eastern European lithosphere as seen by S receiver functions, *Geophys. J. Int*., 181, 604-634.

· Heit., B. (2005), Chapter 4–The Altiplano Plateau, from *Teleseismic tomographic images of the Central Andes at 21˚ S and 25.5˚ S*, submitted for dissertation at Freie Universität Berlin.

· Heit, B., F. Sodoudi, X. Yuan, M. Bianchi, and R. Kind (2007), An S receiver function analysis of the lithospheric structure in South America, *Geophys. Res. Letters*, 34, L14307.

· Helmberger, D.V. and J.E. Vidale (1988), Modeling strong motions produced by earthquakes with two-dimensional numerical codes, *Bull. Seis. Soc. Am*., 78, 109-121.

· Husker, A., I. Stubailo, M. Lukac, V. Naik, R. Guy, P. Davis, and D. Estrin (2008), WiLSON: The Wirelessly Linked Seismological Network and Its Application in the Middle America Subduction Experiment, *Seis. Res. Lett.,* 79 (3), 438-443.

· Julià, J., M., Assumpção, and M.P. Rocha (2008), Deep crustal structure of the Paraná Basin from receiver functions and Rayleigh-wave dispersion: Evidence for a fragmented cratonic root, *J. of Geophys. Res*., 113, B08318.

· Kennett, B. (1991), The removal of free surface interactions from three-component seismograms, *Geophys. J. Int*., 104, 153-163.

· Kim, Y., R.W. Clayton, and J.M. Jackson (2010), Geometry and seismic properties of the subducting Cocos plate in central Mexico, *J. Geophys. Res*., 115, B06310.

· Kumar, P., X. Yuan, R. Kind, and G. Kosarev (2005), The lithosphere-asthenosphere

boundary in the Tien Shan-Karakoram region from S receiver functions – evidence of continental subduction, *Geophys. Res. Lett*., 32, L07305.

· Langston, C. (1979), Structure under Mount Rainier, Washington, inferred from teleseismic body waves, *J. Geophys. Res*., 84, 4749–4762.

· Liggoria, J., and C. Ammon (1999), Iterative deconvolution and receiver function estimation, *Bull. Seism. Soc. Amer*., 89, 19–36.

· Lloyd S., van der Lee, S., Sand Franca, G., Assumpcao, M. & Feng, M., 2010. Moho map of South America from receiver functions and surface waves, *J. of Geophys. Res*., 115, B11315.

· Lucente, F., N.P. Agostinetti, M. Moro, G. Selvaggi, and M. Bona (2005), Possible fault plane in a seismic gap area of the southern Apennines (Italy) revealed by receiver function analysis, *J. of Geophys. Res*., 110, B04307.

· McGlashan, N., L. Brown, and S. Kay (2008), Crustal thickness in the central Andes from teleseismically recorded depth phase precursors, *Geophys. J. Int*., 175, 1013-1022.

· Myers, S., S. Beck, G. Zandt, and T. Wallace, (1998), Lithospheric-scale structure across the Bolivian Andes from tomographic images of velocity and attenuation for P and S waves, *J. of Geophys. Res*., 103 (21),233–21,252.

· Ocola, L.C., J. Leutgert, L.T. Aldrick, R.P. Meyer, and C.E. Helsey (1995). Velocity structure of the coastal region of southern Peru from seismic refraction/wide-angle reflection data, *J. Geodynamics*, 20,1-30.

· Savage, M. (1998), Lower crustal anisotropy or dipping boundaries? Effects on receiver functions and a case study in New Zealand, *J. of Geophys. Res*., 103, B7,

15069-15087.

· Schenk, T., G. Müller, and W. Brüstle (1989), Long-period precursors to pP from deep-focus earthquakes: the Moho underside reflection pMP, *Geophys. J. Int.*, 98, 317-327.

· Somerville, P., R. Graves and N. Collins (2008), Ground Motions from Large Cascadia Subduction Earthquakes, URS Final Report, Award Number: 06HQGR0160.

· Sumner, R. (1967), Attenuation of Earthquake Generated P Waves along the Western Flank of the Andes, *Bull. Seis. Soc. Amer.*, 57 (2), 173-190.

· Vidale, J., D.V. Helmberger, and R.W. Clayton (1985), Finite-difference seismograms for SH waves, *Bull. Seis. Soc. of Amer.*, 75 (6), 1765-1782.

· Whitman, D., B.L. Isacks, J. Chatelain, J. Chiu, and A. Perez, (1992), Attenuation of High-Frequency Seismic Waves Beneath the Central Andean Plateau, *J. Geophys. Res.*, 97, B13, 19,929-19,947.

· Zhang, J. and C. Langston (1995), Dipping Structure under Dourbes, Belgium, Determined by Receiver Function Modeling and Inversion, *Bull. of the Seis. Soc. Amer.*, 85 (1), 254-268.

· Zhang, Z. and T. Lay (1993), Investigation of Upper Mantle Discontinuities Near Northwestern Pacific Subduction Zones Using Precursors to sSH, *J. Geophys. Res.*, 98 (B3), 4389-4405.

· Zhao, L. and D.V. Helmberger (1994), Source Estimation from Broandband Regional Seismograms, *Bull. Seis. Soc. Amer.*, 84 (1), 91-104.

· Zheng, Y. and T. Lay (2006), Low Vp/Vs ratios in the crust and upper mantle beneath

the Sea of Okhotsk inferred from teleseismic p_MP, s_MP, and s_MS underside reflections from the Moho, *J. Geophys. Res.*, 111, B01305.

· Zhu, L. and D.V. Helmberger (1996), Advancement in Source Estimation Techniques Using Broadband Regional Seismograms, *Bull. Seis. Soc. Amer.*, 86 (5), 1634-1641.

· Zhu, L., and H. Kanamori (2000), Moho depth variation in southern California from teleseismic receiver functions, J. Geophys. Res., 105 (B2), 2969–2980.